# Comparisons of Three Global Models of Earth's Magnetosphere During Quiet Geomagnetic Times

Molly K. Williams
molly_williams131@mymail.eku.edu

Eastern Kentucky University

# Comparisons of Three Global Models of Earth's Magnetosphere During Quiet Geomagnetic Times

Molly Williams
Submitted
in Partial Fulfillment
of the
Requirements of HON 420
Fall 2013

By
Molly Williams

Dr. Jessica Lair
Department of Physics and Astronomy, Eastern Kentucky University
Dr. Xianzhe Jia
Atmospheric, Oceanic and Space Sciences, University of Michigan—Ann Arbor

**Abstract**

The Space Weather Modeling Framework (SWMF) at the Center for Space Environment Modeling (CSEM) at the University of Michigan is a powerful tool for modeling space weather and space physics phenomena in the Earth-Sun system. The Block-Adaptive Tree Solarwind Roe-type Upwind Scheme (BATS-R-US), Ionospheric Electrodynamic, and Inner Magnetospheric models within SWMF can be coupled to assess a number of quantities related to the dynamics of the earth's magnetosphere. The basic MHD model—referred in the work as the "Ideal MHD model"—in use is the coupling of BATS-R-US with IE, however IM models are being added to form a global MHD model. Currently, there are two different IM models for this purpose: the Rice Convection Model and the Comprehensive Ring Current Model. This paper assesses the differences between the three couplings and lays a foundation for future comparisons. Cross correlation values between coupling efficiency and cross polar cap potential and polar cap area are carefully considered in the comparison as are time variation plots of each of these values. Contour plots each hemisphere are made for each model and run time and are also considered in the analysis. These plots contain field-aligned currents and Hall and Pedersen conductivities overplotted on the open-closed field line boundary and electric potential values.

*Keywords and phrases:* Magnetosphere, Magnetospheric Modeling, Inner Magnetosphere, Center for Space Environment Modeling, Comprehensive Ring Current Model, Rice Convection Model, Undergraduate Thesis, Honors Thesis

## Table of Contents

## List of Figures

## List of Tables

## List of Commonly Used Abbreviations

| | |
|---|---|
| SWMF | Space Weather Modeling Framework |
| CSEM | Center for Space Environment Modeling |
| SW | Solar Wind |
| IMF | Interplanetary Magnetic Field |
| $R_E$ | Earth Radii |
| CE | Coupling Efficiency |
| FAC | Field-Aligned Currents |
| IM | Inner Magnetosphere |
| OM | Outer Magnetosphere |
| GM | Global Magnetosphere |
| IE | Ionospheric Electrodynamics |
| MHD | Magnetohydrodynamics |
| OCB | Open-closed field line boundary |
| CPCP | Cross polar cap potential |
| BATS-R-US | Block-Adaptive Tree Solarwind Roe-Type Scheme |
| RCM | Rice Convection Model |
| CRCM | Comprehensive Ring Current Model |
| FokRC | Fok ring current (model) |
| RIM | Ridley Ionosphere Model |
| MLT | Magnetic Local Time |
| CON | Control Module |

**Acknowledgements**

This paper is the result of a twelve week Research Experience for Undergraduates (REU) program funded by the National Science Foundation. The research was carried out at the Atmospheric, Oceanic and Space Sciences (AOSS) department in the College of Engineering at the University of Michigan--Ann Arbor. I would like to thank my mentor on this project, Dr. Xianzhe Jia, a research scientist at AOSS, for his guidance during my time at the University of Michigan.

I would also like to thank my honors thesis mentor at Eastern Kentucky University, Dr. Jessica Lair, for taking the time to review my paper and listening to my complaints and concerns throughout the process.

# 1. Introduction

Just outside the Earth's atmosphere, streams of ionized plasma originating from the sun, called the solar wind (SW), collide with the earth's magnetic field. So important is the solar wind that it can be said to be the main factor dominating the properties of the near-earth plasma medium in the magnetosphere and ionosphere. The solar wind has its own associated magnetic field—referred to as the interplanetary magnetic field (IMF)—which ineracts with the magnetic field of the Earth at a boundary called the magnetopause. At this boundary, the SW dynamic pressure and magnetic pressure of the Earth's magnetic field are in equilibrium. The part of the near-earth space environment that is governed by the Earth's magnetic field is called the magnetosphere. On the Earth's dayside, ions in the SW hit the Earth at a direct angle, resulting in a compression of the Earth's magnetic field and a supersonic wave (bow shock) is formed at distance that ranges 2-3 $R_E$ (Earth radii) in front of the magnetopause. At the bow shock, the ions become heated and slow down and are then deflected around the Earth. This results in a magnetosphere with a parabolic shape with the nightside of the magnetosphere having a much larger elongated area which is referred to as the magnetotail. The dayside radius of the Earth's magnetosphere is only about 6-10 $R_E$ while the nightside extends outwards to upwards of 1000 $R_E$.

The magnetosphere is critical because it deflects the majority of heavily charged particles coming from the sun and other cosmic sources that are constantly bombarding the Earth. Magnetospheric modeling can tell researchers much about the basic properties of the magnetosphere and can lead to a better understanding of the physical processes governing its interactions with other parts of the near-Earth space environment and the magnetosphere's own fundamental processes. Moreover, magnetospheric modeling can describe many aspects of space

weather which affects a multitude of technology as well as the launching of space shuttles and instruments. Instruments for communications, navigation (GPS), meterology, and defense systems operate within this region and are subject to any disturbances that might occur. Certain domains in the near-Earth system can use simplifying assumptions about the interactions of that domain with the entire system and thus can be simulated with stand-alone models. Other times, satellite and ground-based measurements can give insight into the effects of such domains. However, in order to predict space weather events with accuracy, the use of coupled physics based models are usually necessary.

The modeling of the global magnetosphere requires this coupled approach. The magnetosphere is a highly complex multi-scale system with its characteristic components ranging in size scales from hundreds of kilometers, like the electron gyro radius at about 100 km, to hundreds of earth radii. Plasma processes within the magnetosphere also range from electron processes to the global plasma behavior. Modeling the magnetosphere usually requires the use of multiple models to describe the dynamic and multi-scale nature of the magnetosphere itself.

In the realm of large scale theoretical modeling, the Earth's magnetosphere is often divided into two parts, the inner magnetosphere and the outer magnetosphere. The inner magnetosphere (IM) typically includes all field lines that extend to about 8 $R_E$ while the outer magnetosphere can extend todistances of hundreds of thousands $R_E$ . Conditions in the outer magnetosphere can be described with single-fluid magnetohydrodynamics (MHD) equations. The main pressure bearing particles in the inner magnetosphere are highly energetic (1-200 keV) ions from the inner plasma sheet and ring current. For these particles, $\mathbf{E} \times \mathbf{B}$ (drift velocity) is typically slower than gradient and curvature drift, which is proportional to particle energy (*De*

*Zeeuw, 2004*).Thus small-scale, non-MHD plasma proccesses are key in describing the dynamics in this region of the magnetosphere (*De Zeeuw, 2004*).

Traditionally, two different types of models have been used to model these main pressure bearing particles: "ring current models" and "convection models". Magnetic and electric fields are taken as input in ring current models. In contrast convection models use magentic fields as input and calculate IM electric fields self-consistently. Ring current models typically follow particles with different values of the first and second adiabatic invariants and calculate energy and pitch angle; loss is considered carefully by exchange and preciptation. In contrast, isotropic pitch angle distrubutions which treat $H^+$ and $O^+$ together are typically used in convection models. In these models, loss is either neglected or is calculated separately in less detail than ring current models.

A coupling of two models--one to model the outer magnetosphere and one to model the inner magnetosphere--can be used to get a more complete and acurate global magnetospheric model. The boundary between these two regions is located near the open-closed magnetic field line boundary (OCB) and thus the properties of this region are important in assessing the quality of these couplings. The outer region uses only an MHD model while the IM region is modeled with a coupling of an MHD model and either a ring current or convection model. Results of the global MHD model depend upon the interaction of "driving" solar wind with a magnetized spherical representation of the Earth.

At the Center for Space Environment Modeling, (CSEM), the Space Weather Modeling Framework (SWMF) carries out the modeling and coupling of numerous domains in the near-Earth space environment. The most basic coupling for global magnetosphere (GM) modeling at CSEM is the Block-Adaptive Tree Solarwind Roe-type Upwind Scheme (BATS-R-US) with the

ionospheric electrodynamics (IE) model, the Ridley Ionosphere Model (RIM). Currently, this coupling can be combined with two different inner magnetosphere (IM) models, the Rice Convection Model (RCM) and Comprehensive Ring Current Model (CRCM), to form a more comprehensive magnetospheric model. SWMF carries out the modeling and coupling of numerous domains in the near-Earth space environment. In this work, I assess the differences between these three different GM models and provide an overview of each of the couplings being consideration.

## 2. The Space Weather Modeling Framework (SWMF)

Space weather and space physics modeling at the University of Michigan is performed through the Space Weather Modeling Framework (SWMF). The SWMF is a software framework that consists of a collection of various physics-based space weather simulations and space physics applications. SWMF has been designed in order to be versatile, achieve good parallel performance, and integrate physics modules with small changes. In general, this framework incorporates numerical models in 12 domains of the Sun-Earth system. These components are: Solar Corona (SC), Lower Corona (LC), Solar Energetic Particles (SP), Inner Heliosphere (IH), Outer Heliosphere (OH), Polar Wind (PW), Radiation Belts (RB), Ionospheric Electrodynamics (IE), Eruptive Event Generator (EE), Inner Magnetosphere (IM), Global Magnetosphere (GM), and Upper Atmosphere (UA). There are currently two more components of SWMF currently under development--the Plasma Sphere (PS) and Lower Atmosphere (LA) numerical models. Each model differs from the other in their grid structure, equations of evolution, and variables for input and output; however, some models do overlap in the physical domain and can interact through a boundary surface.

The beauty of the SWMF is the ability to couple models together to create multiple domain simulations. The SWMF can combine multiple domains into one component as long only one of the combined domains is coupled to the rest of the components (*Tòth, et al., 2005*). Each of the physics domains correspond to a modeling component within the framework. The different components in the SWMF interact through the use of standardized interfaces between them. Each component within the SWMF, such as those in the IM domain, can have different variations with their own physical model, wrappers and couplers. These wrappers and couplers are Fortran 90 codes written to be component interfaces. In this case, the wrapper is an interface with the Control Module (CON) and provides the standard interface for interaction; the coupler is an interface between components which performs data exchange.

Each component is stored in a library and linked back to the core of the framework so that the libraries are shared to form a single executable. The components are then distributed over a parallel machine for execution and coupling (*Tòth, et al., 2012*). Input parameters in the SWMF are controlled by a single input parameter file that allows the SWMF to maintain a certain ease of use that other modeling frameworks might not have. New domains can be added by either incorporating them into already existing components or by creating a completely new domain and adding it to the framework library.

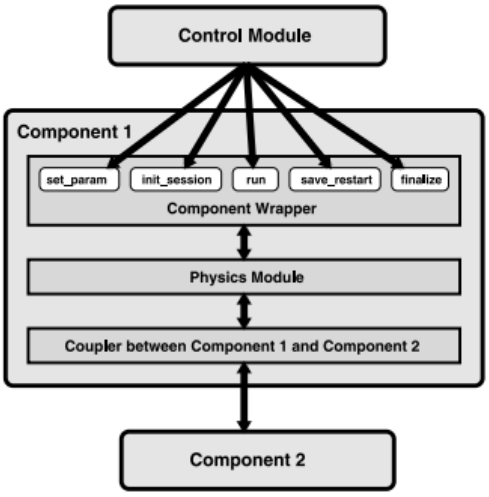


**Figure 2.** The structure of a physics component.

**Figure 1**. SWMF component structure (*Tòth, et al., 2005*)

The SWMF user creates a layout file which contains information about which components the framework should couple for each run. At initialization, the SWMF stores this information and the CON assigns a Message Passing Interface communication group based on the processor layout. If the layouts for two components over lap, then they progress in a sequential time-shared manner. If they do not overlap, then they run concurrently. Input parameters are read from a single XML file with special tags to mark component specific parameters. The SWMF has two different sessions (time accurate and steady-state) that control execution that both initialize the components and couple them for the first time. After the initial coupling, components only communicate when necessary. At the end of the sessions, final plot files are written out, log files are closed, and performance and error reports are printed.

# 3. Global MHD Models and Couplings

## 3.1 Block-Adaptive Tree Solarwind Roe-type Upwind Scheme (BATS-R-US) and Ionospheric Electrodynamics (IE) Coupling

The original BATS-R-US code began as a MHD simulation code for space physics applications, but was later coupled with other models. BATS-R-US models the GM, EE, LC, SC, IH, IE and OH components of the SWMF, but the SWMF user can select for BATS-R-US to run any of these components separately as well. There are currently 37 equation modules and 42 user modules to choose from in BATS-R-US leading to a wide range of customization and variability for the user (*Tòth, et al., 2012*). BATS-R-US can be used to study a variety of physical phenomena--from cometary heliospheres to coronal mass ejections. Current runs of BATS-R-US are executed using the GM component along with IE component modeled with the Ridley Ionosphere Model (RIM), a 2D spherical ionospheric potential solver which uses fully parallel latitude slices. This coupling is commonly referred to as the "Ideal MHD" model.

As it stands today, BATS-R-US is a multi-domain, global MHD model which is capable of solving various forms of ideal single-fluid MHD equations including Hall, semi-relativistic, multi-species and multi-fluid MHD, anisotropic pressure, radiative transport and heat conduction (*Tòth, et al., 2012*). Due to the difficulty in solving these equations, BATS-R-US represents the most computationally expensive model within the framework. The governing equations of ideal MHD BATS-R-US seeks to solve the continuity, momentum, and heat balance equations together with Faraday's Law, Ampere's law, and Ohm's law. The equations, as stated in Buzulukova et al published in 2010 (see references page) are:

$$\frac{\partial \rho}{\partial t} + \mathbf{u} \cdot \nabla \rho + \rho \nabla \cdot \mathbf{u} = 0$$

$$\rho \frac{\partial \mathbf{u}}{\partial t} + \rho \mathbf{u} \cdot \nabla \mathbf{u} + \nabla \mathbf{p} - \mathbf{j} \times \mathbf{B} = 0$$

$$\frac{\partial \rho}{\partial t} + \mathbf{u} \cdot \nabla \mathbf{p} + \gamma \mathbf{p} \nabla \cdot \mathbf{u} = 0$$

$$\mathbf{j} = \frac{1}{\mu_0} \nabla \times \mathbf{E} = 0$$

$$\frac{\partial \mathbf{B}}{\partial t} + \nabla \times \mathbf{E} = 0$$

$$\mathbf{E} = -\mathbf{u} \times \mathbf{B}$$

These ideal MHD equations are solved across a range of plasma (β) values with a finite volume discretization using the conservative variables magnetic field (**B**), momentum density (ρ**u**), density (ρ), and total energy density (*e*) as noted in a paper by De Zeeuw and others in 2004. These equations are rewritten in conservative form for the eight dimensional vector, $\mathbf{U} = [\rho,\ \rho\mathbf{u},\ \mathbf{B},\ \epsilon]^{\mathbf{T}}$ consisting of total energy density, momentum density, magnetic field, and density using

$$\frac{\partial \mathbf{U}}{\partial t} + \ (\nabla \cdot \mathbf{F})^{\mathrm{T}} = \mathbf{S}$$

where $\mathbf{S} \propto \nabla \cdot \mathbf{B}$ is the source term and **F** is the flux tensor.

The computational domain of the Ideal MHD model extends from 32 $R_E$ upstream (dayside) to 224 $R_E$ downstream (nightside) of the planet. The sides of the magnetosphere domain are equivalent at 64 $R_E$. The inner MHD boundary is located at 2.5 $R_E$ with plasma density n=28 $cm^{-3}$ and T=25000 K (*Buzulukova et al., 2010).* SW conditions are treated as boundary conditions at the upwind boundary of the simulation domain (*De Zeeuw, et al., 2004*) and, along with IMF parameters, are used to calculate outer boundary conditions at $X_{GSM}$ =32

$R_E$. In order to enforce the MHD constraint $\nabla \cdot \mathbf{B} = \mathbf{0}$, different divergence control schemes are implemented which include: the eight-wave scheme; the diffusive/parabolic approach; the projection scheme; and a conservative form of the constrained transport scheme (*De Zeeuw et al., 2004)*. At the inner boundary, field-aligned currents $(\mathbf{J}_{||})$ in the ionosphere at 3.5 $R_E$ are calculated using

$$\mathbf{J}_{||} = (\nabla \times \mathbf{B}) \cdot \mathbf{b}$$

where $\mathbf{b}$ is the local magnetic field. The values calculated for the field-aligned currents in BATS-R-US are then fed into the RIM in order to calculate the electric potential and map it onto the IE component grid. Field-aligned currents are mapped to the ionosphere for use in the RIM using the dipolar (background) magnetic field and scaled according to

$$\mathbf{B}_i / \mathbf{B}_{3.5}$$

with $\mathbf{B}_i$ being the ionospheric magnetic field and $\mathbf{B}_{3.5}$ being the magnetic field at 3.5 $R_E$.

Once a height-integrated conductance pattern is generated, the electric potential is solved by a preconditioned gradient reduction resolution (GMRES) solver using

$$\mathbf{J}_R(\mathbf{R}_i) = [\nabla_\perp \cdot (\Sigma \cdot \nabla\psi)_\perp]_{R_i}$$

which describes the relationship between the height-integrated conductance tensor, $\Sigma$, the ionospheric potential, $\psi$, and the radial component of the current, $\mathbf{J}_R$**.** The RIM solves the potential in each hemisphere independently with zero potential at a latitude 5º lower than the lowest latitude field-aligned current. This electric potential ($\Phi$) is then mapped back to the inner boundary of the GM grid (usually at about 2.5 $R_E$) using the background magnetic field. Electric fields and corresponding plasma velocities at the inner boundary are then calculated using the relationships

$$\mathbf{E} = -\nabla\psi$$

$$\mathbf{V} = \mathbf{E} \times \mathbf{B}/_{B^2}$$

The corrotation velocity field is then added to the ionosphere generated velocity field.

BATS-R-US uses a 3D block-adaptive grid with blocks of the same number of cells, but different sizes in physical space. The grid resolution varies from $^1/_8$ $R_E$ in the IM to 4 $R_E$ near the outer boundary of the simulation domain. Higher resolution in the IM is used necessary for accurate field-line tracing used in the IM couplings (discussed below). In most cases, blocks sizes and volumes are anywhere between 64 (4x4x4) cells and 1728 (12x12x12) cells. This block scheme allows the grid resolution to be automatically refined. Blocks began at equal resolution. However, in regions where a resolution increase is necessary a "parent" block is refined by dividing itself into eight "child" blocks which contain the same number of cells as the parent. If a region is over-resolved this process is reversed and the "child" blocks are combined into a single "parent" block in order to half the cell resolution. Time stepping information is contained in "ghost cells" associated with each block. Generalized coordinates are used in conjunction with Cartesian vector components so that equations are kept in Cartesian form and only the geometry of the grid is altered (*Tòth, et al., 2012*). With these features, a number of grid schemes are available to use including spherical, cylindrical, toroidal, and even arbitrarily stretched grids.

### 3.2 Rice Convection Model (RCM), BATS-R-US and IE Coupling

While the BATS-R-US and IE coupling discussed previously models the outer region and inner boundary conditions of the GM. In order to have a complete global MHD model, the Rice Convection Model (RCM) is one of two IM models that can be coupled along with the basic BATS-R-US/IE coupling. These two models are coupled to produce more realistic region-2

field-aligned currents through a better representation of gradient and curvature drift physics in the IM. The RCM, developed for over 30 years at Rice University in Houston, is a large numerical code created to describe the electrodynamics of the coupled inner magnetosphere-ionosphere system. RCM modeling usually extends from just outside the magnetopause on Earth's dayside to the middle of the plasma sheet at about 25 $R_E$-- a region characterized by closed magnetic field lines and slow flowing plasma.

As discussed previously, single-fluid MHD equations can not be used to describe the dynamics of the inner magnetosphere. The RCM can not specify the particle source and sink boundary conditions, but does compute the electric field self-consistently. For the coupling processes the RCM is treated as a module of the global MHD code with BATS-R-US providing the driving inputs for RCM. By assuming isotropic particle distribution plasma motion can be represented as the motion of a whole flux tube and local plasma populations are represented by a collection of about 100 different fluids. Each fluid is characterized by an index, s, which specifies a given energy invariant and chemical species and by energy invariant $\lambda_s$, charge $q_s$ and flux tube content $\eta_s$ (the number of particles per unit magnetic flux). These quantites are related to the kinetic energy, $W_s$, and the number density $n_s$ through the flux tube volume

$$V = \int \frac{ds}{B}$$

through the relation

$$\lambda_s = W_s V^{2/3}$$

Each fluid is advected using

$$\frac{\partial \eta_s}{\partial t} + \frac{\mathbf{B} \times \nabla \left( \Phi + \Phi_c + \left( \frac{\lambda_s}{q_s} \right) V^{-2/3} \right)}{B^2} \cdot \nabla \eta_s = -L$$

where $\Phi$ is the electric potential in the ionospheric electric potential which rotates with the earth, $\Phi_c$ is the corotation potential which converts $\Phi$ to a non rotational frame, and L represents explicit loss. Boundary conditions to compute this value are usually taken from statistical plasma sheet models. Field-aligned current in the RCM is calculated via

$$\mathbf{J}_{||i} = \frac{1}{2}\hat{b} \cdot \nabla V \times \nabla P$$

with $\mathbf{J}_{||i}$ as the current densityinto the northern ionosphere, $\hat{b}$ is a unit magnetic field vector, and the right side is evaluated at the ionosphere. Initial and boundary conditions for the plasma flux tube contents ($\eta$) are required for the computation of $\mathbf{J}_{||i}$**.** BATS-R-US MHD model provides mass density ($\rho$) and pressure, P, which are treated as moments of the distribution function of an assumed shape in the RCM in order to calculate these conditions. This computes the set of $\eta_s$values for both electrons and protons everywhere in the RCM region or only along the outer RCM boundary.

The total particle pressure, P, is given by

$$P = \frac{2}{3}V^{-5/3}\Sigma_s\lambda_s\eta_s$$

Potential distribution is determined from the condition of conservation at the ionosphere via

$$\nabla \cdot \left[-\overleftrightarrow{\Sigma} \cdot \nabla\Phi + \mathbf{j}_w\right] = \mathbf{J}_{||i} \sin(I)$$

where $\nabla$ is acting upon the 2D ionospheric spherical shell, I is the dip angle of the magnetic field below the horizontal plane and $\mathbf{j}_w$ is the ionospheric current driven by neutral winds. Ionospheric potential is given by the IE model and mapped to the RCM grid. This mapping is achieved by calculating equatorial crossing of magnetic field lines that originate from the RCM ionosphere grid points. The elements of $\overleftrightarrow{\Sigma}$, a 2 x 2 conductance tensor, are expressed through field line

integrals or Pederson and Hall conductivities extending through all the ionosphere. In order to compute the above equation, the potential on the high-latitude boundary is taken from BATS-R-US. The conductance used in RCM are the same as those used in BATS-R-US. When the RCM is coupled to BATS-R-US and the IE model, zero Hall conductance and uniform Pederson conductance of 4 S in each hemisphere is assumed.

Coupling of BATS-R-US and RIM (the Ideal MHD model) to the RCM is complicated. Solutions obtained with the BATS-R-US and IE coupling are obtained on a 3D computational grid (described previously) while RCM quantities are calculated on a 2D ionospheric grid. The basic MHD model calculates fieldline volume, field line mass, field line pressure, and equatorial plane temperature which must be translated to the 2D RCM map. Both the most important and the most computationally difficult parts of the coupling is the 3D to 2D mapping and inverse transformations that rely on globally performed tracing magnetic field lines.

An accurate and effiecient method for tracing the magnetic field lines is necessary for computing the basic model quantites to send to the RCM and to send the RCM computed pressures back to the basic BATS-R-US/IE model.The magnetic field lines are traced within each block of BATS-R-US adaptive grid (described above). Once end and beginning field line points are known for each block, an exchange of information takes place between neighboring blocks and their shared faces through the use of ghost cells so that the blocks now contain tracing information about the field lines in a larger volume of physical space. This process continues until the tracing information does not change. Traces with both ends on the ionosphere are deemed close field lines and are considered for coupling to the RCM. At this point, each cell need only trace its outer edge to determine the exact latitude and longitude mapping of its magnetic field line through interpolation. Thus, the open-closed field line boundary is mapped to

the RCM grid. Once the RCM has run, the total particle pressure can easily be mapped back to the MHD grid since each cell already knows its mapping location.

### 3.3 Comprehensive Ring Current Model (CRCM), BATS-R-US, and IE Coupling

.

The third model coupling assessed in this work is the CRCM/BATS-R-US/IE coupling. The CRCM is the second IM model and is itself a kinetic model coupling of the RCM model (discussed above) and the Fok Ring Current (FokRC) using the RCM Birkeland current algorithm with an arbitrary pitch angle distribution. In general, the FokRC seeks to solve the bounce-averaged Boltzmann equation for a number of particle species, s, described by the two adiabatic invariants in the FokRC which are M, the relativistic magnetic moment, and K defined as

$$K = \frac{J}{\sqrt{8 m_0 M}}$$

where J is a longitudinal invariant and the right side of the equation represents the loss terms due to scattering into the loss cone and charge exchange (*Glocer et al., 2013*).

While the RCM has been discussed above, the FokRC model calculates the plasma distribution by solving the Boltzmann equation for specified **E** and **B** fields; the bounce-averaged Boltzmann transport equation is used to solve for the temporal variation of the 4D phase space density , $\bar{f}_s = \bar{f}_s(\lambda, \phi, M, K)$, for each particle species. In the above equation, $\phi$ and $\lambda$ specify ionospheric coordinates and are the invariant latitude and magnetic local time (MLT), respectively. The bounce-averaged Boltzmann transport equation utilized in the FokRC is:

$$\frac{\partial \bar{f}_s}{\partial t} + \langle \dot{\lambda} \rangle \frac{\partial \bar{f}_s}{\partial \lambda} + \langle \dot{\phi} \rangle \frac{\partial \bar{f}_s}{\partial \phi} = -v \sigma_s \sigma_s \langle n_H \rangle \bar{f}_s - \left( \frac{\bar{f}_s}{0.5 \tau_b} \right)_{loss}$$

where the operator ⟨x⟩ means bounce averaged, v is the velocity of a particle, $n_H$ is a geocorona H density, $\sigma_s$ is a cross change for charge-exchange losses with the geocorona, and $\tau_b$ is a bounce period (*Buzulukova, et al., 2010*). Particle motion in the FokRC is described by the bounce-averaged particle drift velocities--which are the sum of the E × B and gradient curvature drifts- -across field lines assumedly fixed and essentially dipolar labeled by their ionospheric foot prints (*Fok et. al, 2001*).

Coupling the FokRC and RCM allows the CRCM to simulate the evolution of the inner magnetic plasma distribution. Both the RCM and FokRC models utilize an ionospheric grid system with the outer ionospheric boundary in the auroral zone. In order to couple the Fok kinetic model with the RCM, the phase space density from the FokRC output is converted to the RCM's flux tube content ($\eta_s$) and the generalized RCM algorithm is used to calculate the ionospheric potential.

Like the RCM, the CRCM uses a self-consistently calculated electric field. However, the CRCM simulation domain is restricted to the region of closed field lines and extends no further than 15 $R_E$ from the Earth's center. Its overall purpose is to provide a description and simulation of the inner magnetosphere's ring current electrons and ions. The first step in the CRCM is calculating the evolution of the distribution function at each point. This is due to the drift velocities and losses from the FokRC. Next, field-aligned currents in the ionosphere are calculated from a current continuity equation between the magnetosphere and ionosphere:

$$\mathbf{J}_{||\mathrm{i}} = \frac{1}{r_i \cos^2(\lambda)} \sum_s \left( \frac{\partial \eta_s}{\partial \lambda} \frac{\partial W_s}{\partial \phi} - \frac{\partial \eta_s}{\partial \phi} \frac{\partial W_s}{\partial \lambda} \right)$$

with the summation being done at a fixed ( λ, ϕ) over all M, K points. In this context, $\mathbf{J}_{||\mathrm{i}}$ is the sum of ionosphere field-aligned current densities for both the northern and southern

hemispheres, and $W_s$ is the kinetic energy of a particle given by with a given λ, ϕ, M, and K (*Buzulukova et al., 2010*). Here, $\eta_s$ is still the flux tube content, but is now associated with ΔM and ΔK such that

$$\eta_s = 4\sqrt{2}\pi(m_0{}^{3/2})\,\bar{f}_s(\lambda, \phi, M, K)M^{1/2}\Delta M\,\Delta K$$

Once field-aligned currents have been calculated, their distribution is used obtain the ionospheric potential.

The first coupling of the CRCM and ideal MHD model was done by *Buzulukova et al* ( 2010). This paper, however, uses the new two-way coupling of the two models that. The two-way coupling was done using methods from the RCM /Ideal MHD coupling given above and in *De Zeeuz et al* (2004). The CRCM takes the ionospheric potential calculated by the BATS-R-US and RIM (the two coupled components of the Ideal MHD). Magnetic field line traces from the Ideal MHD model with foot prints corresponding to the CRCM grid are then extracted and passed to the CRCM along with equatorial mass density and pressure at the CRCM outer boundary. The CRCM then calculates ring current fluxes along with density and pressure (*Glocer et al, 2013*) and feeds the density and pressure at the minimum magnetic location along the field line to BATS-R-US to use in its IM calculations. In order to pass along information to the CRCM, BATS-R-US determines the ionospheric location of each point in the larger global magnetosphere domain and interpolated the density and pressure to the corresponding CRCM locations.

## 4. Model Output & Analysis

The models in this paper were simulated for January 1, 2001. The number density was held at a constant value of 5.0 ($particles \cdot cm^{-1}$). Temperature was held at a constant 150,000

K. Both the magnetic field and solar wind were varied from north and south directions. Dayside coupling efficiency was calculated by using the formula:

$$\text{C. E.} = \left(\frac{1}{4}\right)|v_x|B_{yz}\sin^2\left(\frac{\theta}{2}\right)$$

where $v_x$ is the x-component of the solar wind, $B_{yz}$ is the magnetic field magnitude in the yz plane, and $\theta$ is the clock angle measured form the +z axis.

The results of the model runs were analyzed for different lengths of time depending upon the models coupled. All couplings had the same start time of 01:05:00 UT and output was generated for every five minutes after the start date. The end time for the BATS-R-US and IE coupling was 10:00:00 UT; 09:20:00 UT for BATS-R-US, IE, and RCM; and 11:00:00 UT for BATS-R-US, IE and CRCM. The direction of the solar wind and magnetic field is given by the orientation of their z axis component; a positive z component indicates northerly direction while a negative z component indicates southerly direction. The driving solar wind is also controlled for the most part by its x component which is two orders of magnitude larger than the y and z SW components. For this model run, the driving solar winds maintain a northward direction. In contrast, the magnetic field is oriented in the southward direction for most of the run before changing quickly to a northern direction around 09:00 UT and dipping quickly back to the southern direction before run completion. This is important because, when the magnetic field is oriented southward, reconnection occurs. That is, "open" flux tubes are formed allowing for the Earth's polar regions to connect with and be affected by interplanetary space. When this occurs, the SW carries open tubes from the day side to the night side and reconnection occurs in the magnetotail's center which releases closed flux tubes towards the earth and back to the day side. This leads to a cyclic flow, called the Dungey cycle, of reconnection both in the magnetosphere

and the ionosphere where it maps. Solar winds were injected ten minutes later than the start time for the model runs. The following plots (Figure 3) show in detail the driving wind, IMF conditions (Figure 3), and coupling efficiency for the model run.

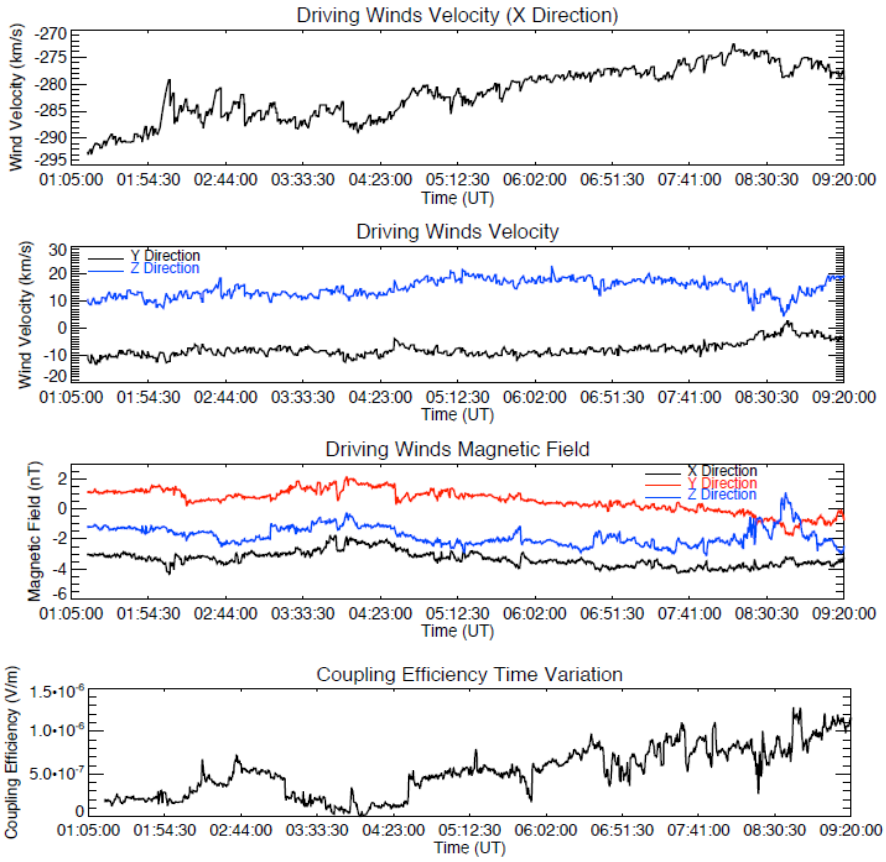


**Figure 2**.Solar wind, IMF, and coupling efficiency over the time interval 01:05:00 UT to 09:20:00 UT.

For each time interval and coupling, a file containing information for that run was generated. Fifteen variables were assessed: (1) co-latitude; (2) longitude; (3) Hall conductivity ($\sigma_H$); (4) Pedersen conductivity ($\sigma_P$); (5) radial component of the current ($J_R$);(6) electric potential ($\Phi$);(7) energy flux; (8) average particle energy; (9) flux to volume ration ($^1/_B$); (10) flux to content ($\rho$); (11) entropy (p); (12) joule heating; (13) ion number flux; (14) conjugate latitude; and (15) conjugate longitude.

From this data output file, polar contour plots were generated that displayed Hall conductivity, Pedersen conductivity, and field-aligned currents (FAC) for each model and hemisphere separately. Also included in these plots were electric potential contour lines, the location of the open-closed field line boundary (OCB), and the polar cap potential drop (CPCP). These figures were used as a qualitative basis for comparison between the three model couplings.

### 4.1 Representative Time Variation Plots

The following 21 pages show the field-aligned currents, Hall conductivities, and Pedersen conductivities for each of the three couplings from 01:05 UT to 09:20 UT. Contour lines detailing electric potential values are over-plotted. The negative potential values are represented by dashed lines while positive electric potential values are overlaid in solid lines. The bold central line represents the location of the open-closed field line boundary for each of the model runs. The dayside of the each hemisphere is located at the top half of the grid. Beginning at the top and going clock-wise, the axis times are noon, dusk, midnight, and dawn. From top to bottom, each page has six FAC plots, followed by six Hall conductance plots, and six Pedersen conductance plots. FAC values range from -0.99 to 0.99, Pedersen conductance values range from 0 to 35.64, and Hall conductance values range from 0 to 39.60. Note that the differences between the northern and southern hemisphere's conductance values are partially due to the seasonal effect as this model was run in the northern winter. In the southern summer, the southern hemisphere is more illuminated and thus background conductance is much higher as is evidenced in the following plot pages.

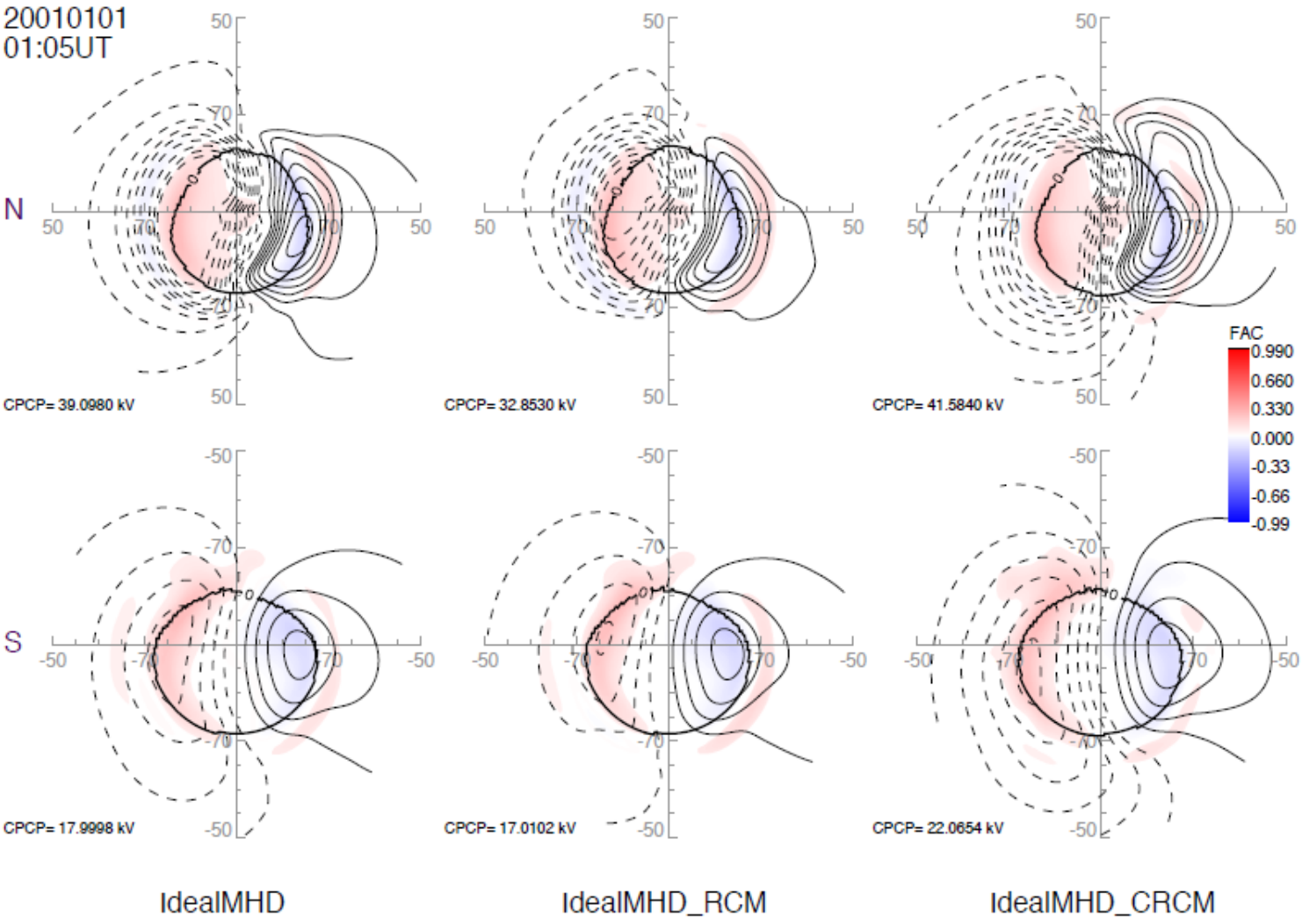


**Figure 3.** FAC values for UT 01:05. Values displayed for each pole and model coupling.

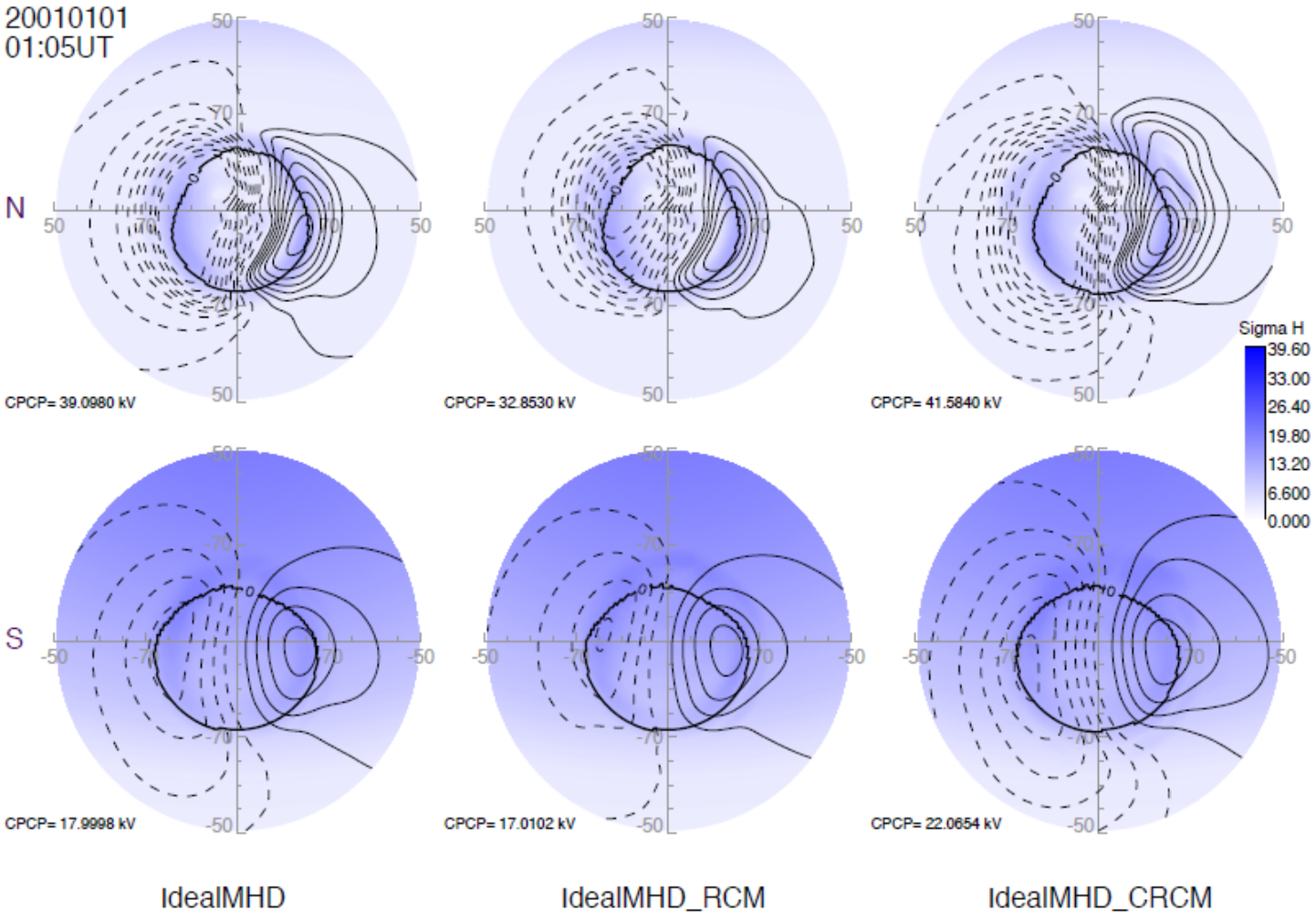


**Figure 4.** Hall conductivity for UT 01:05. Values displayed for each pole and model coupling.

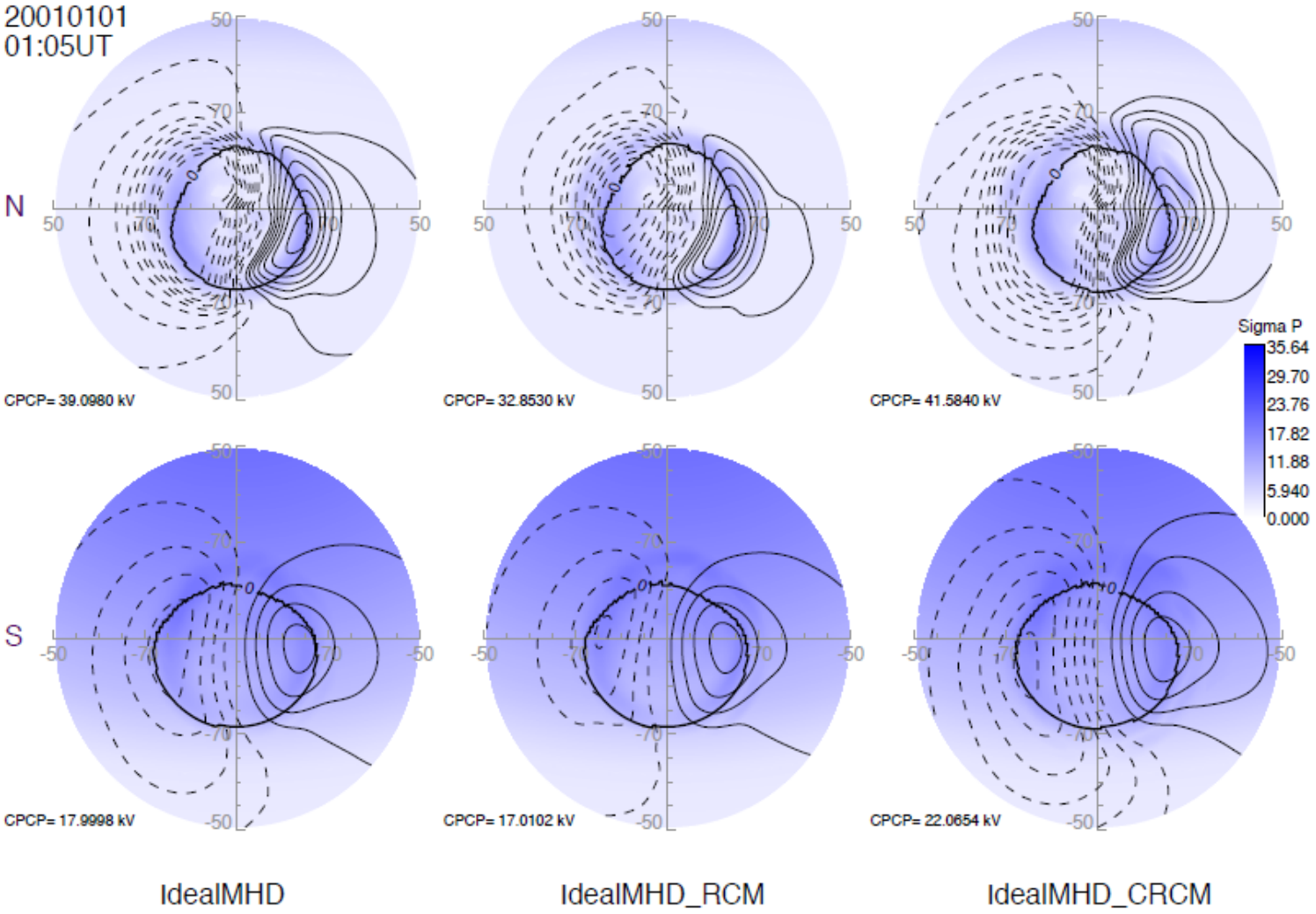


**Figure 5.** Pedersen conductivity for UT 01:05. Values displayed for each pole and model coupling.

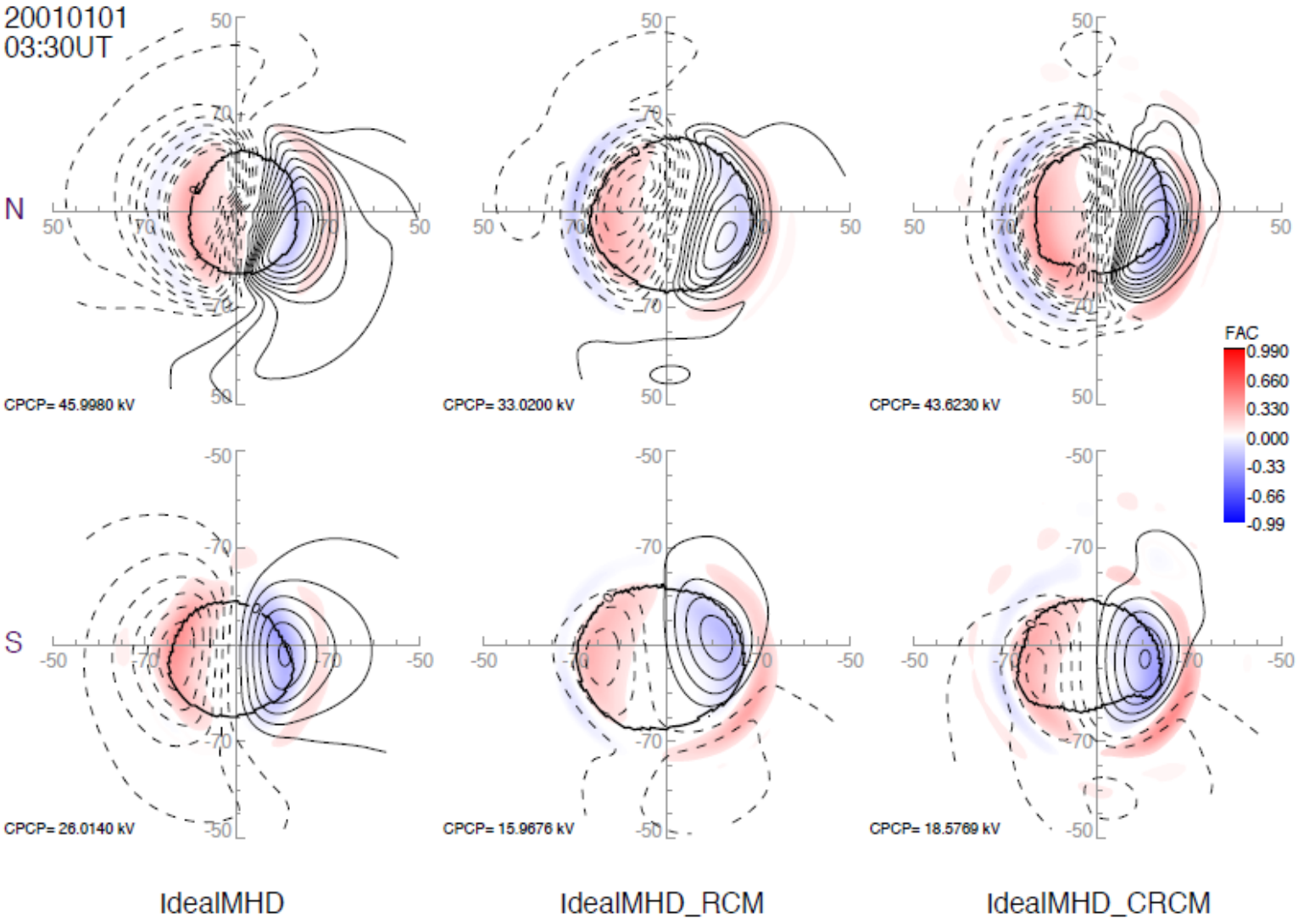


**Figure 6.** FAC values for UT 03:30. Values displayed for each pole and model coupling.

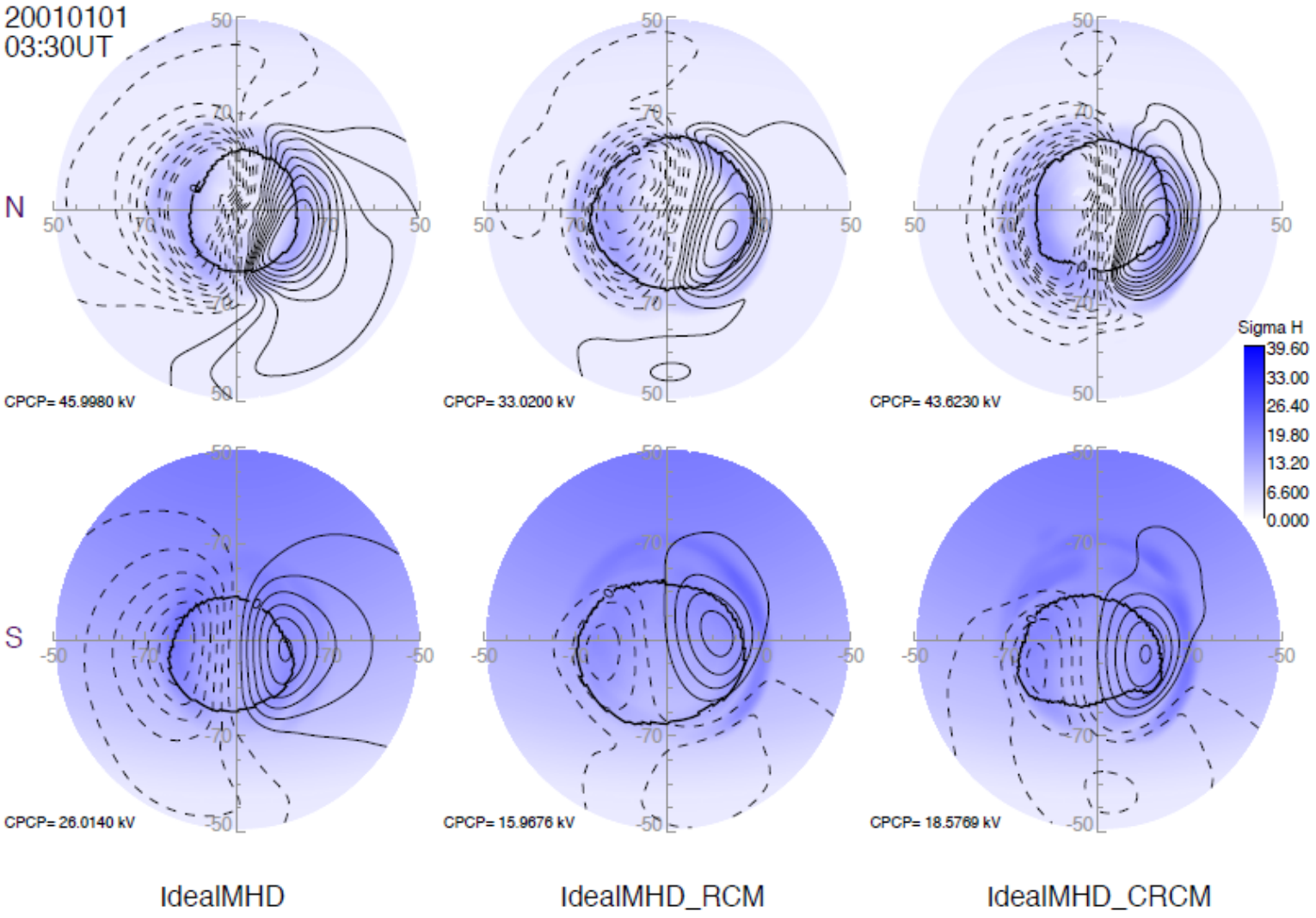


**Figure 7.** Hall conductivity for UT 03:30. Values displayed for each pole and model coupling.

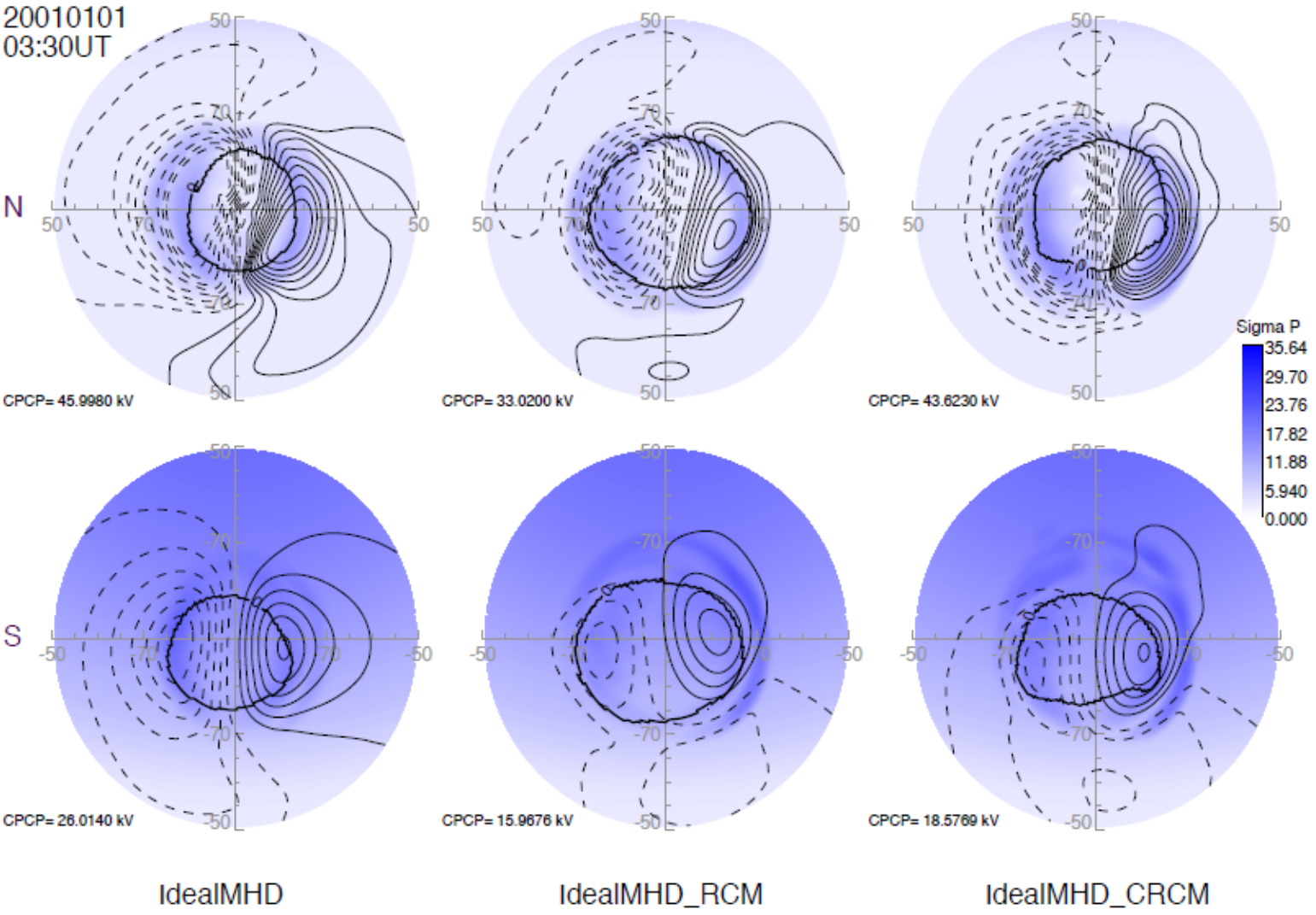


**Figure 8.** Pedersen conductivity for UT 03:30. Values displayed for each pole and model coupling.

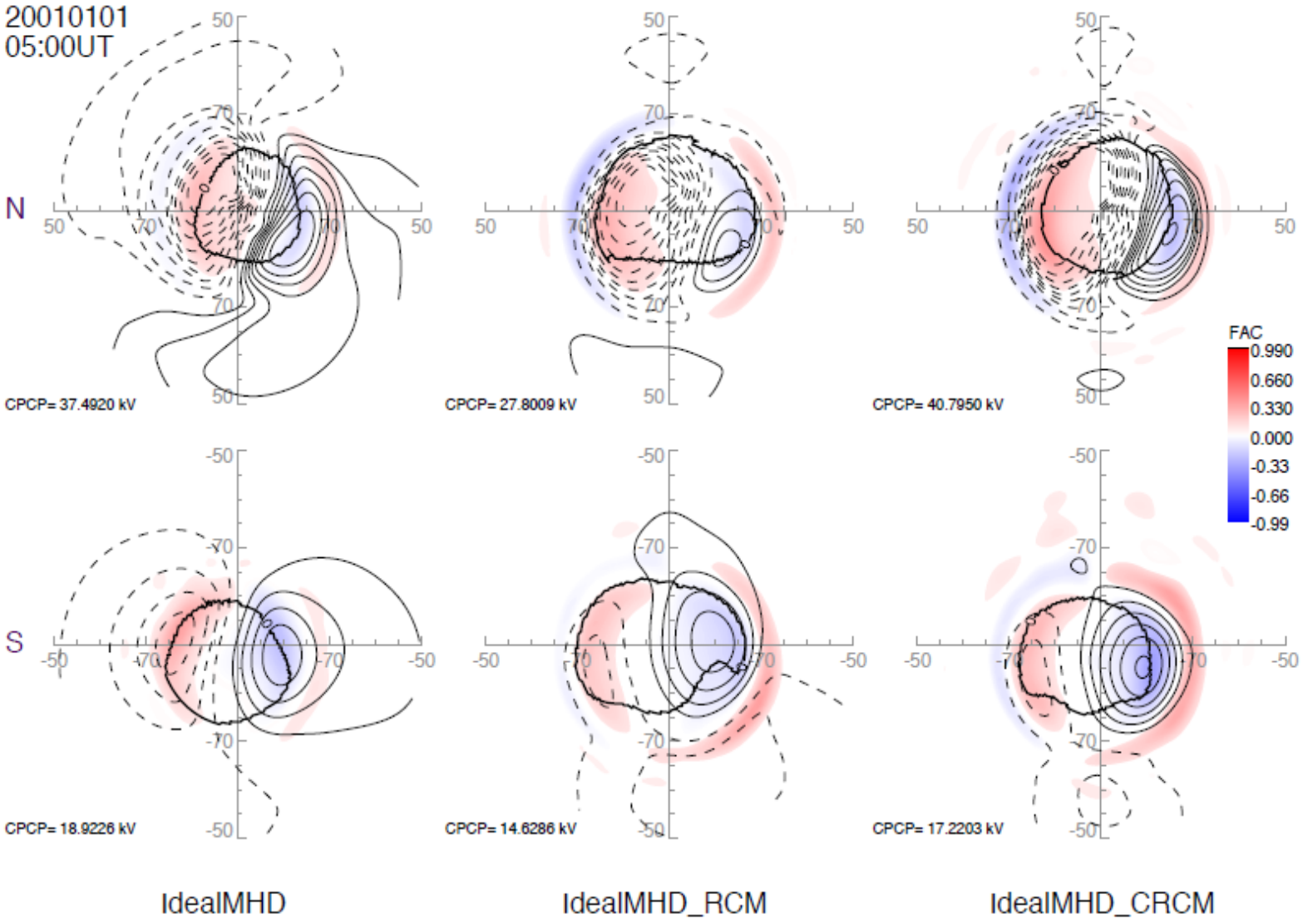


**Figure 9.** FAC values for UT 05:00. Values displayed for each pole and model coupling.

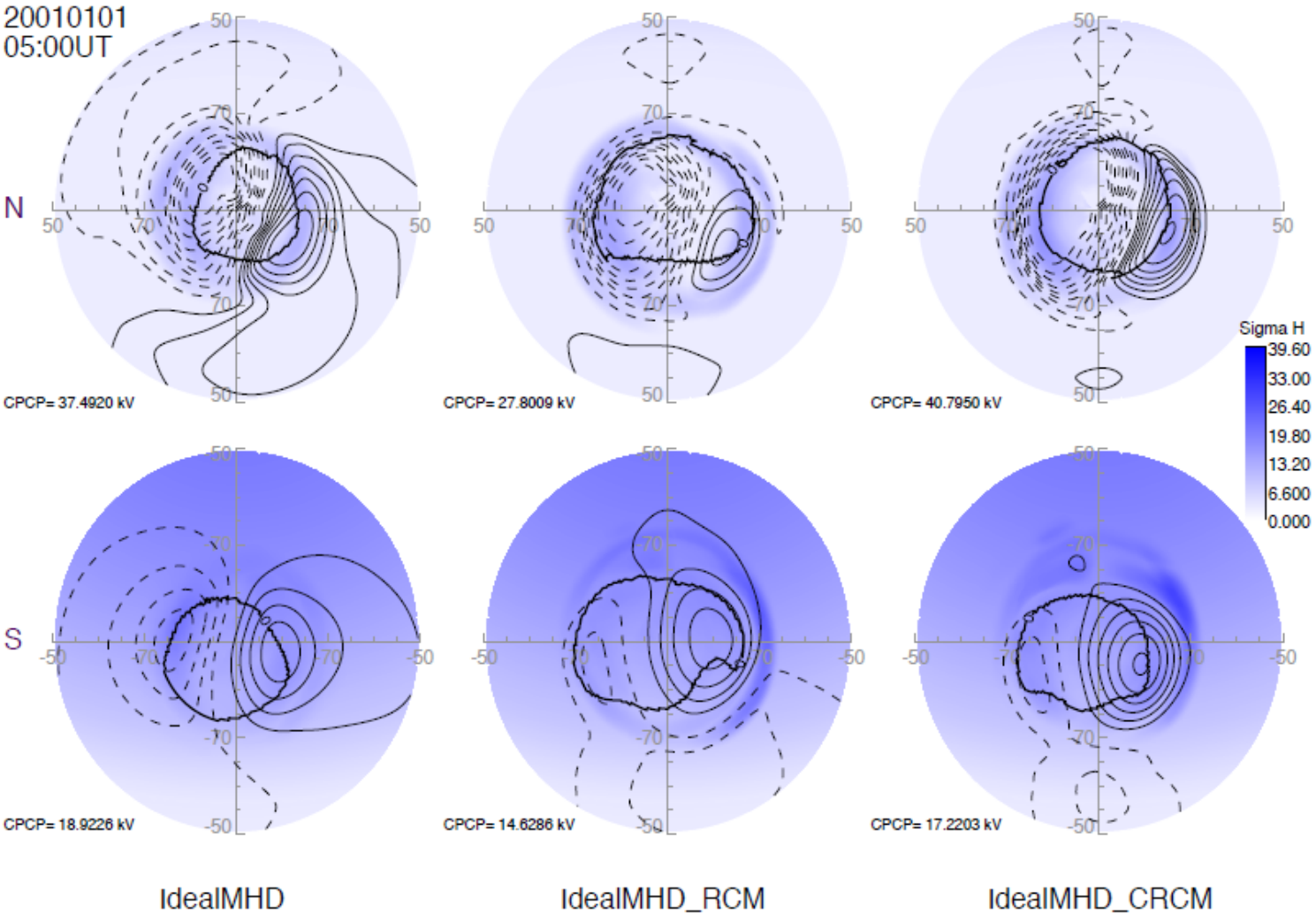


**Figure 10.** Hall conductivity for UT 05:00. Values displayed for each pole and model coupling.

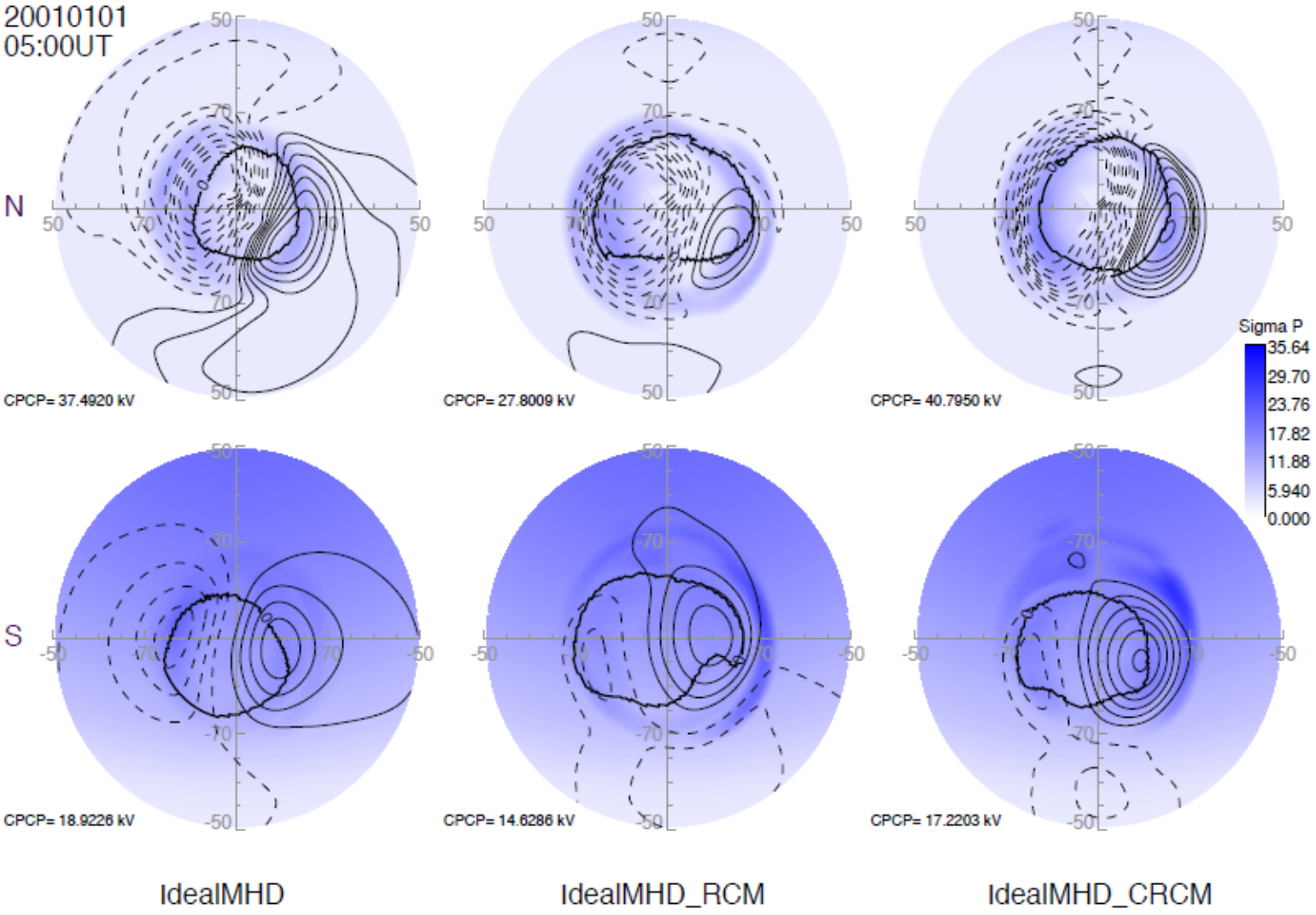


**Figure 11.** Pedersen conductivity for UT 05:00. Values displayed for each pole and model coupling.

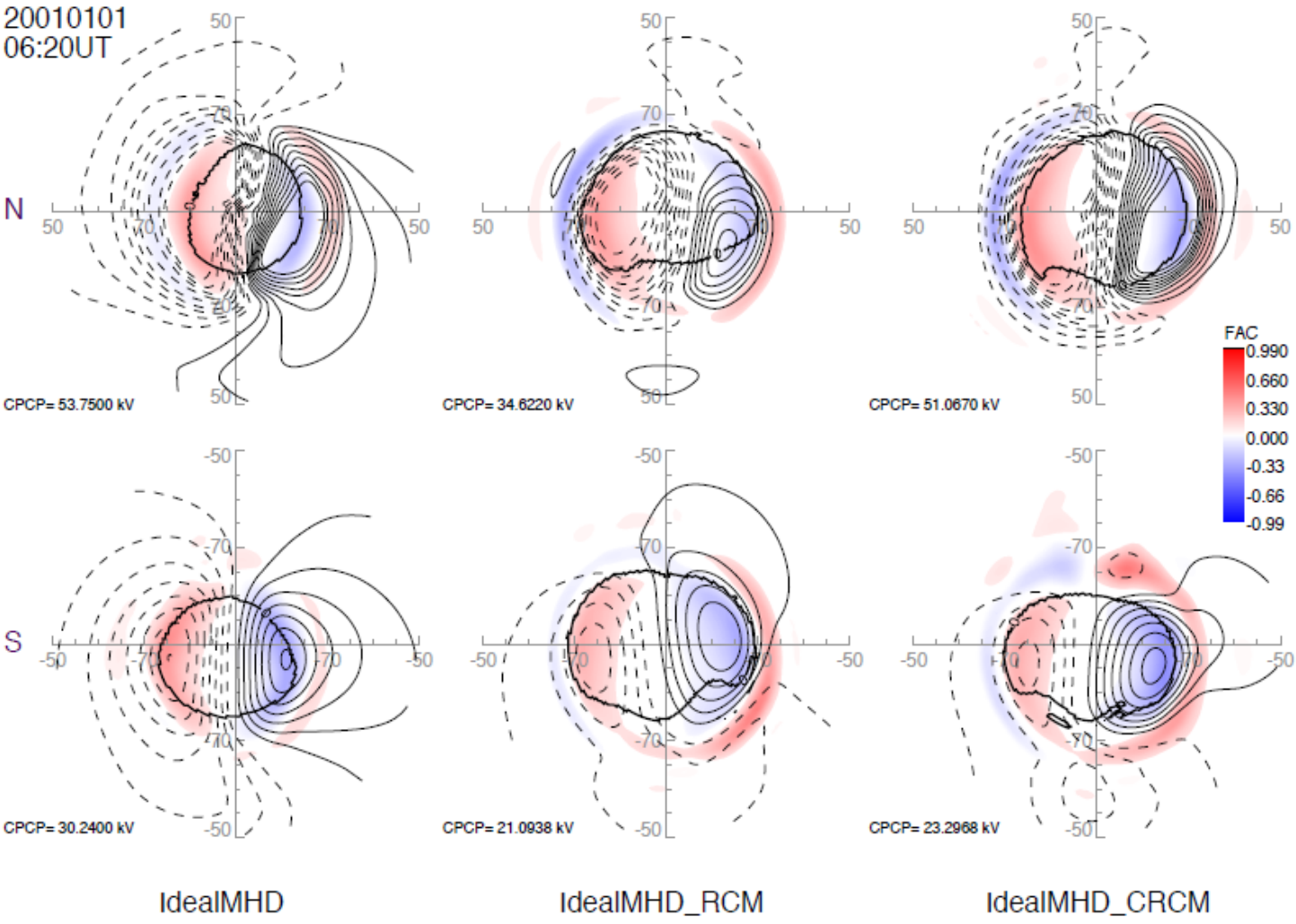


**Figure 12.** FAC values for UT 06:20. Values displayed for each pole and model coupling.

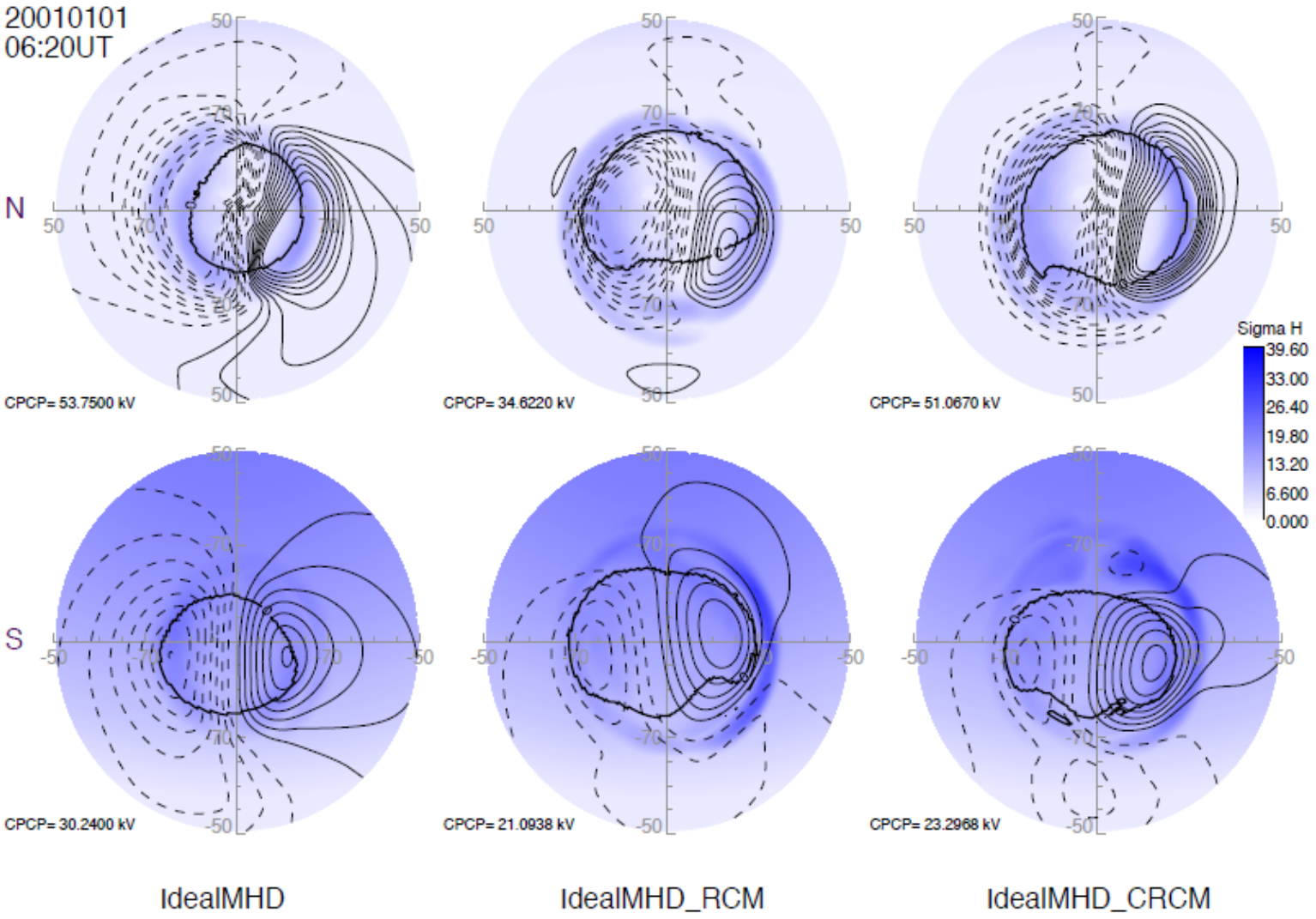


**Figure 13.** Hall conductivity for UT 06:20. Values displayed for each pole and model coupling.

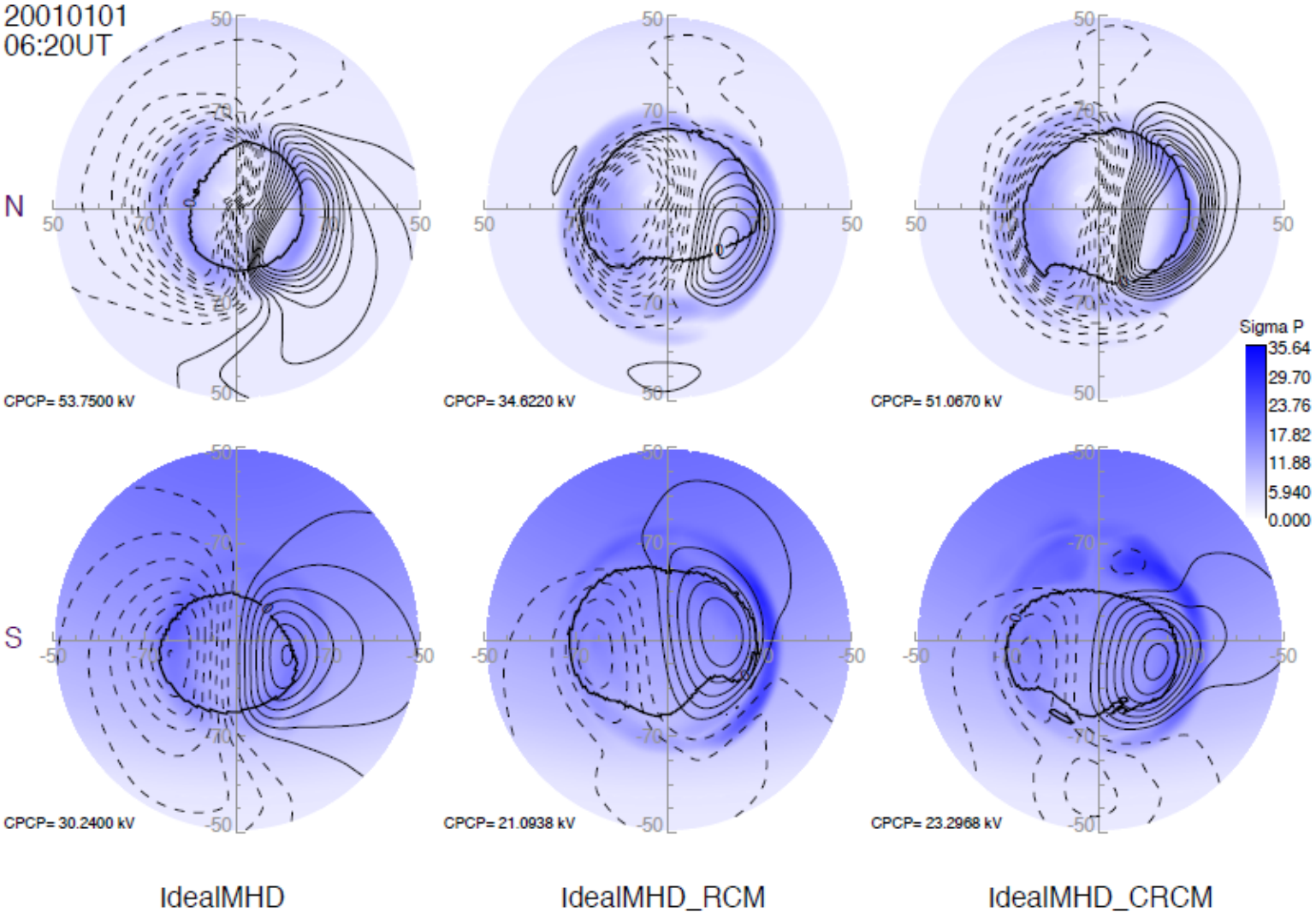


**Figure 14.** Pedersen conductivity for UT 06:20. Values displayed for each pole and model coupling.

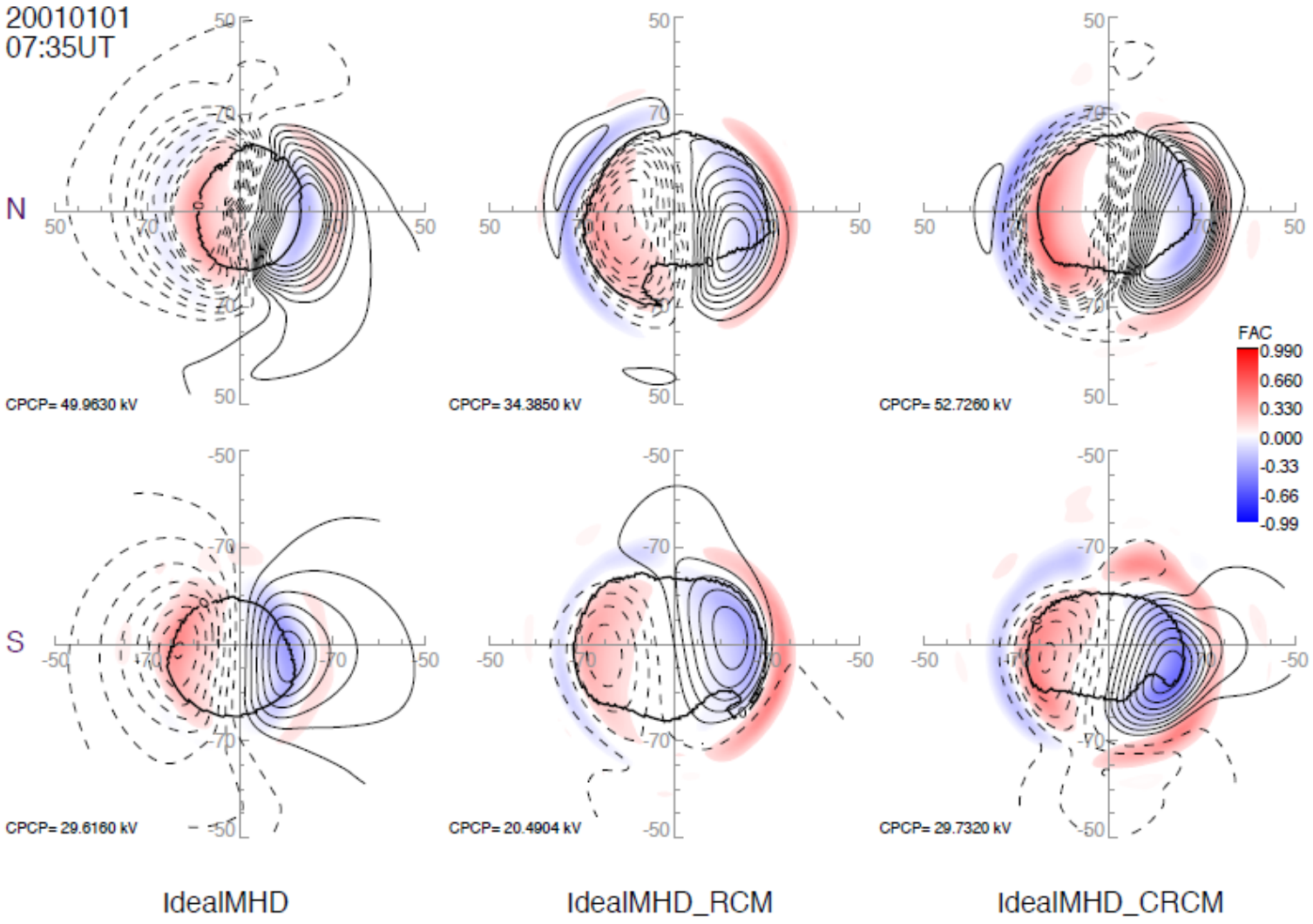


**Figure 15.** FAC values for UT 07:35. Values displayed for each pole and model coupling.

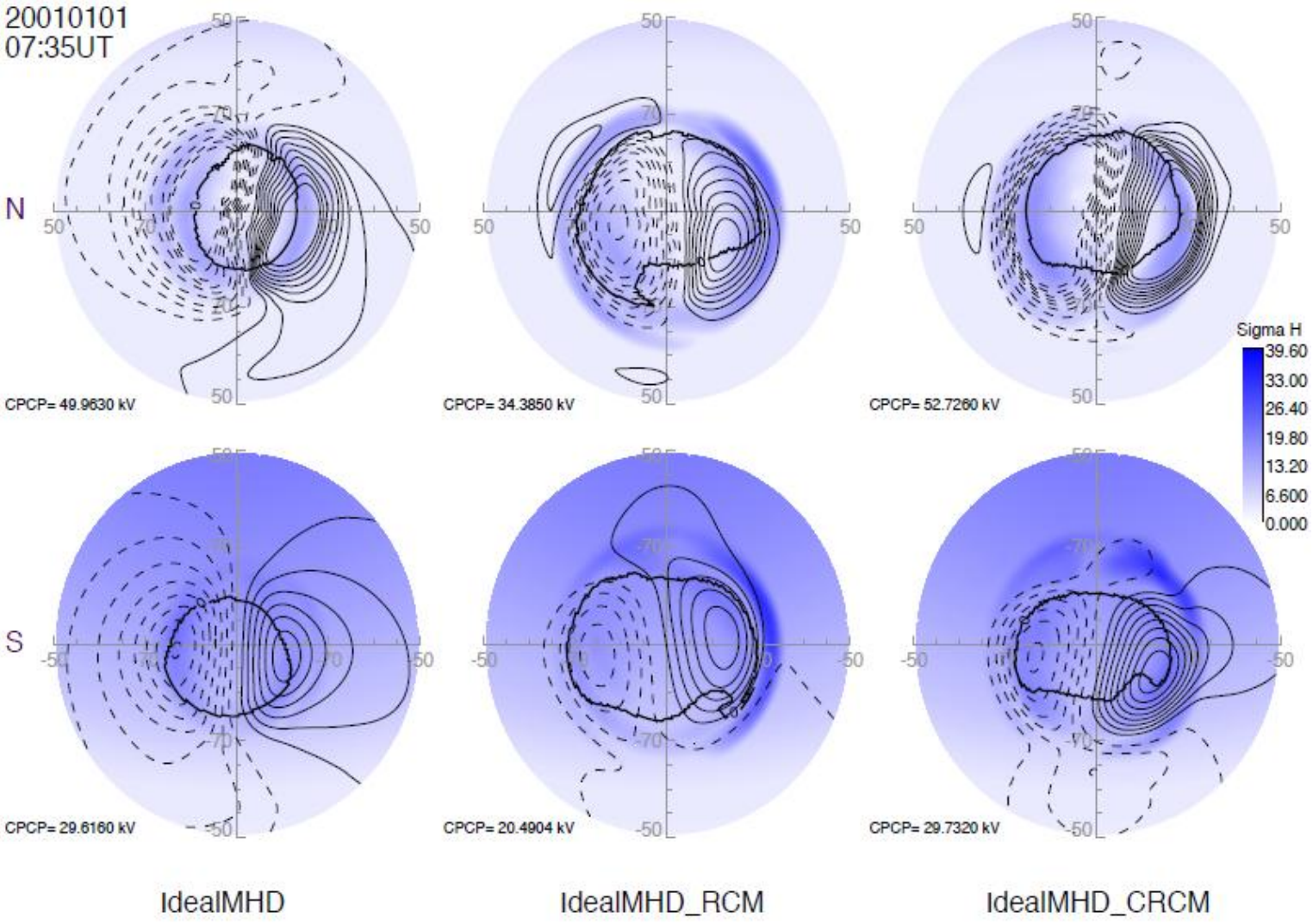


**Figure 16.** Hall conductivity for UT 07:35. Values displayed for each pole and model coupling.

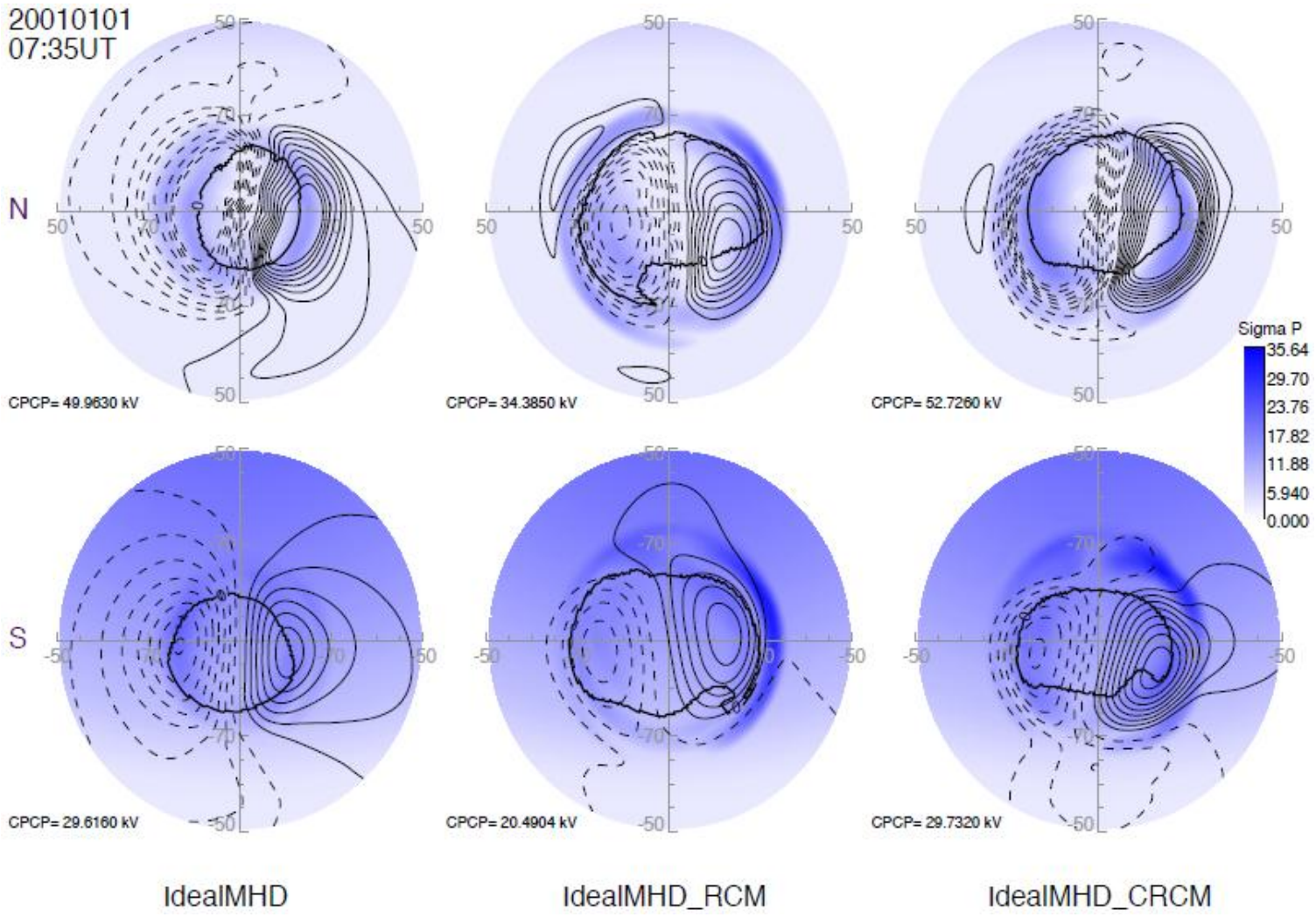


**Figure 17.** Pedersen conductivity for UT 07:35. Values displayed for each pole and model coupling.

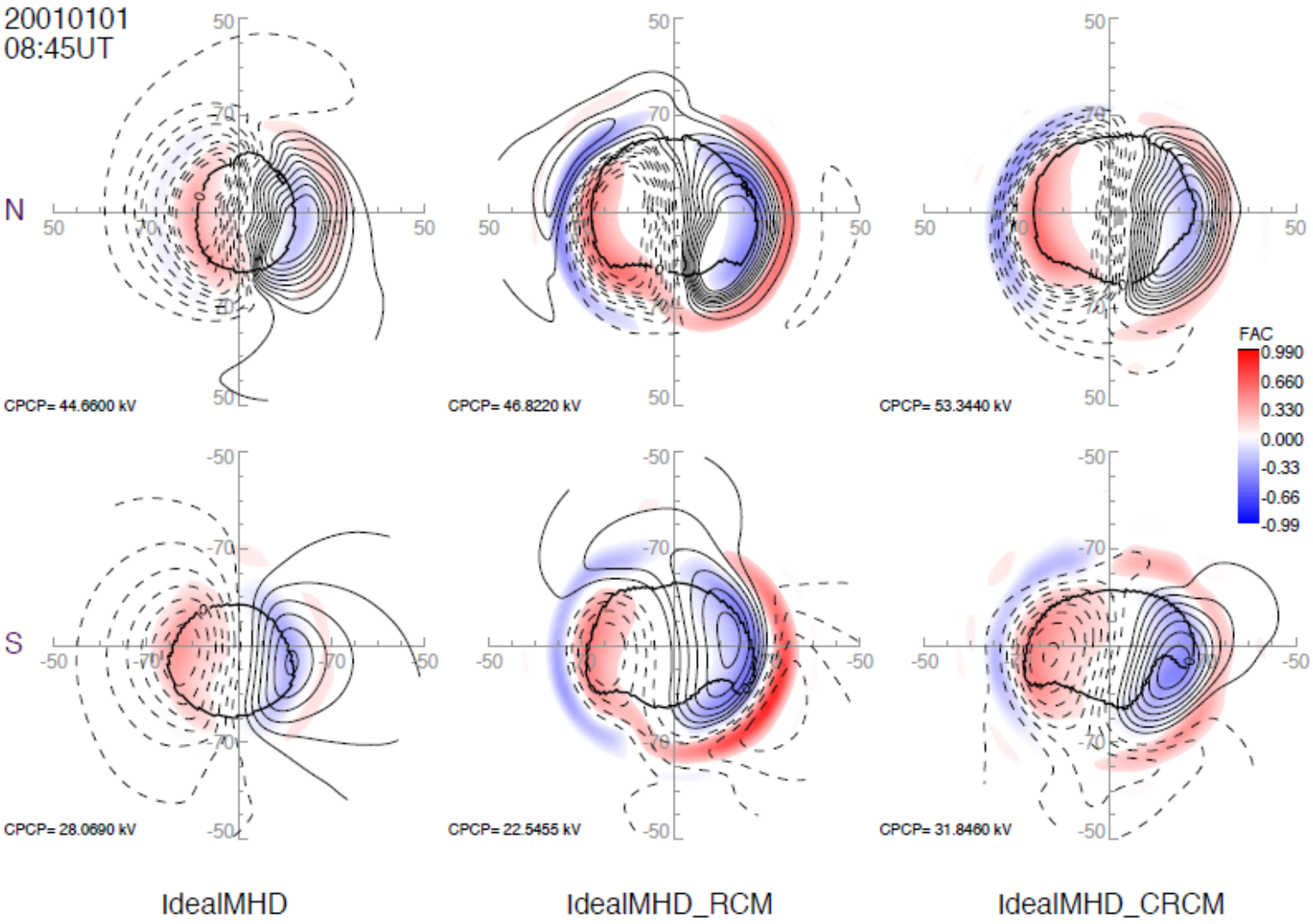


**Figure 18.** FAC values for UT 08:45. Values displayed for each pole and model coupling.

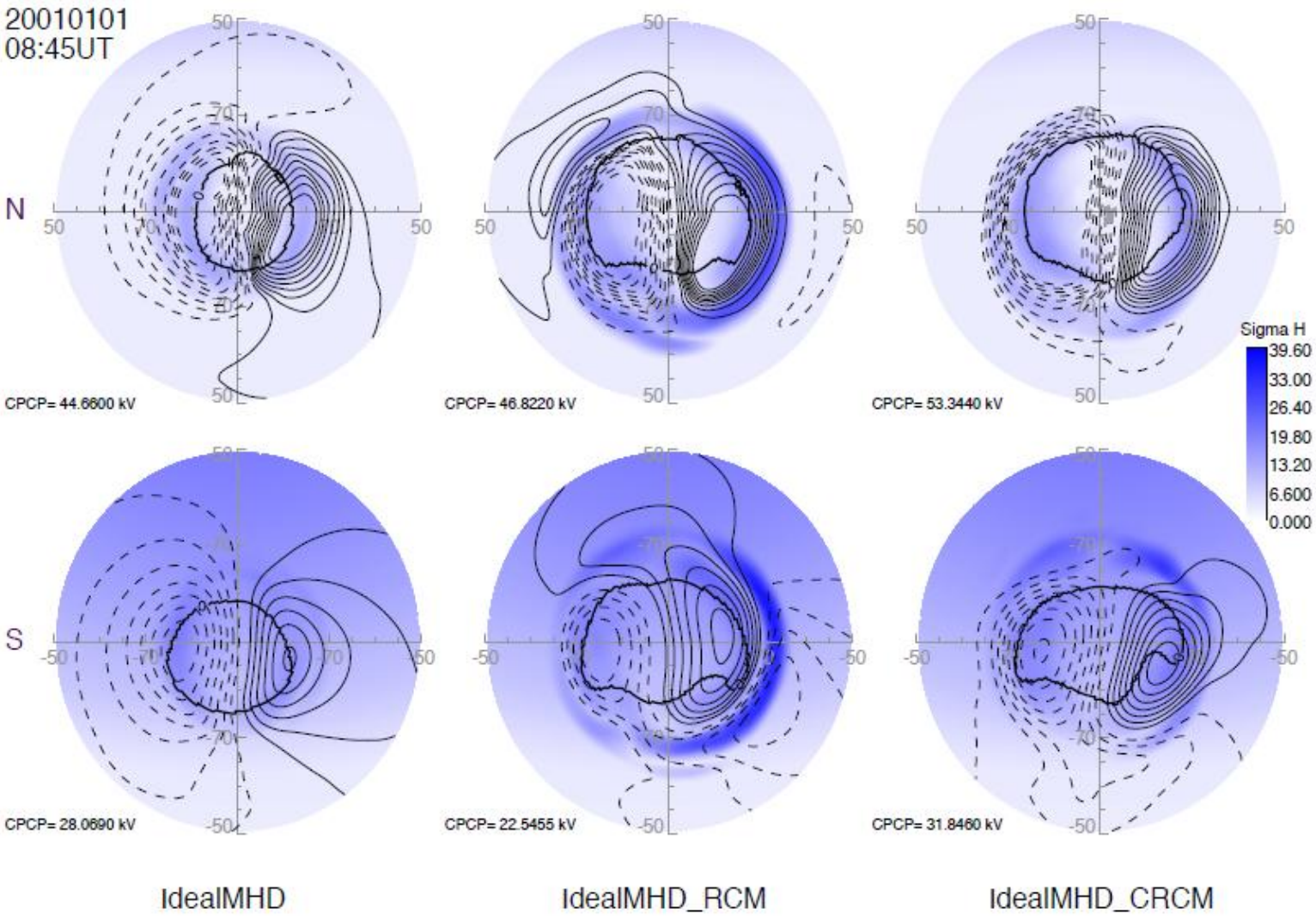


**Figure 19.** Hall conductivity for UT 08:45. Values displayed for each pole and model coupling.

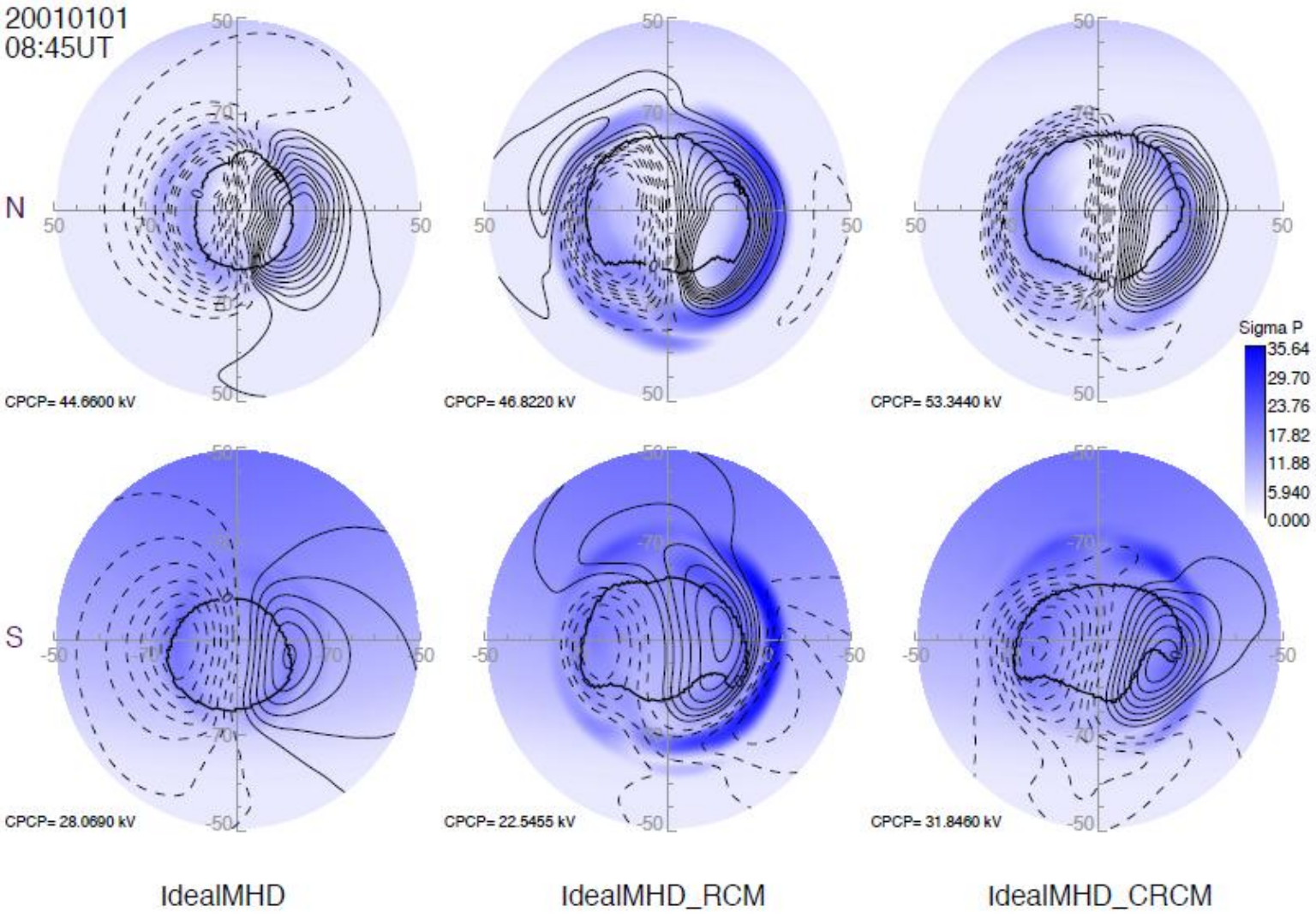


**Figure 20.** Pedersen conductivity for UT 08:45. Values displayed for each pole and model coupling.

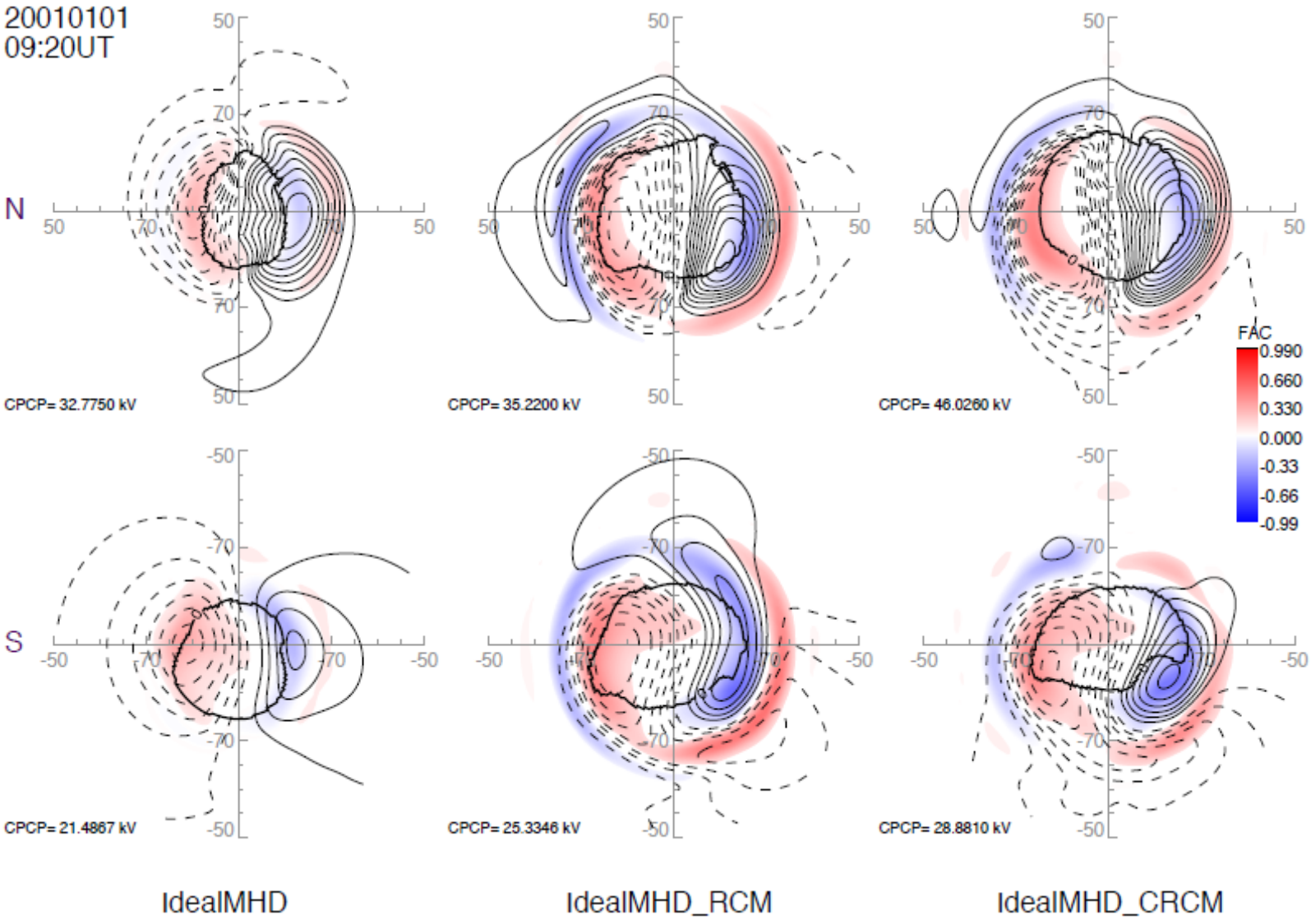


**Figure 21.** FAC for UT 09:20. Values displayed for each pole and model coupling.

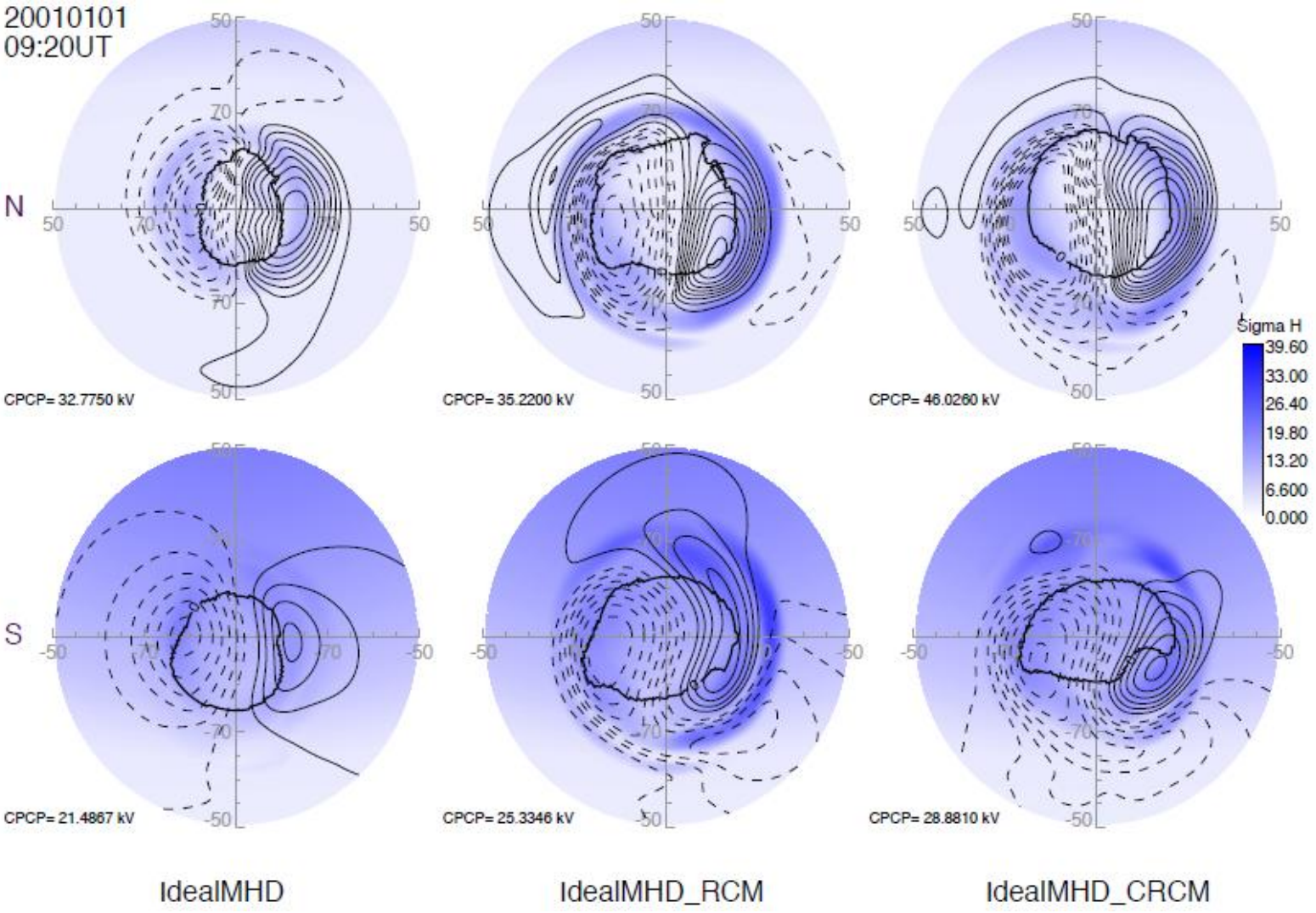


**Figure 22.** Hall conductivity for UT 09:20. Values displayed for each pole and model coupling.

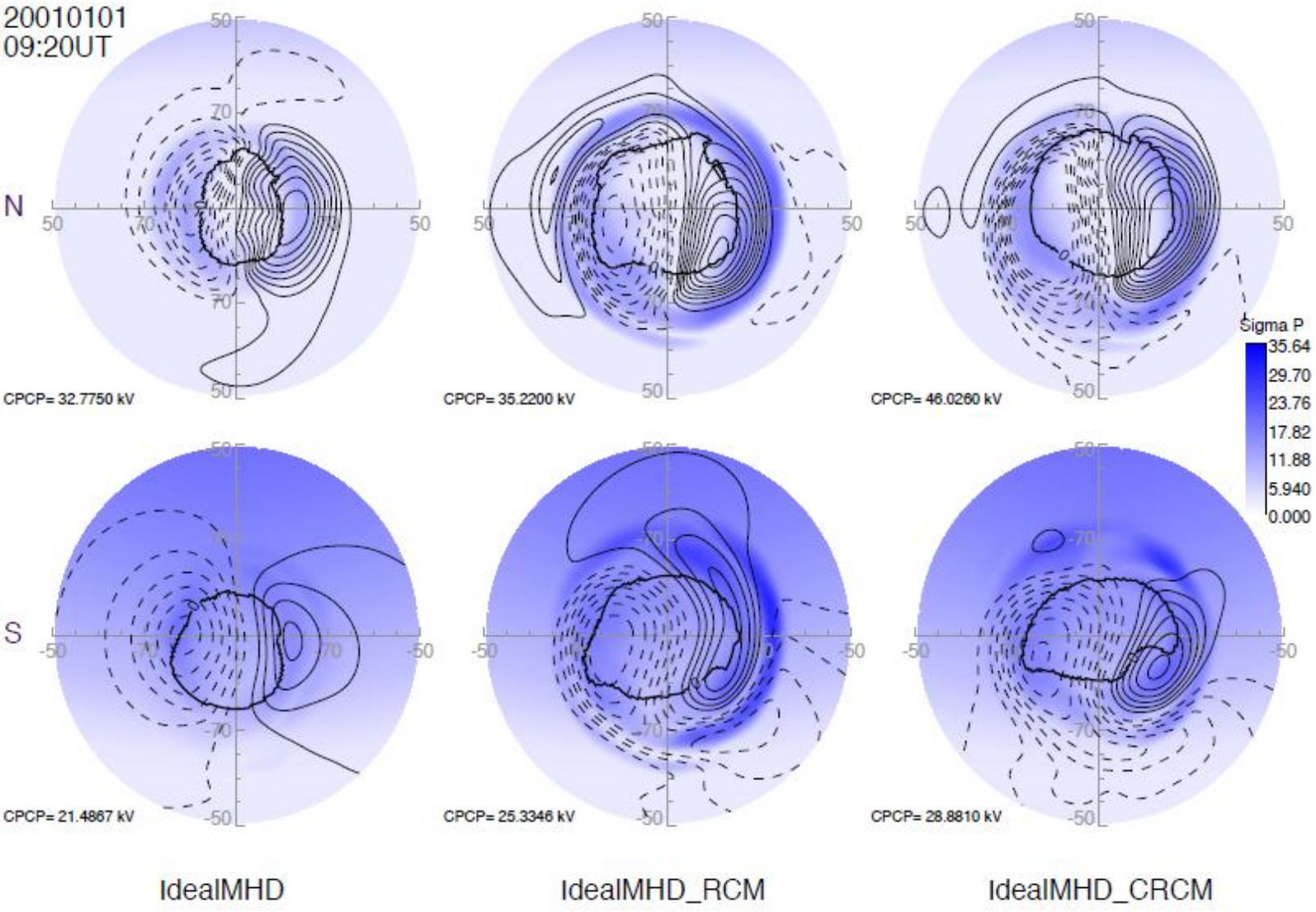


**Figure 23.** Pedersen conductivity for UT 09:20. Values displayed for each pole and model coupling.

The representative contour plots can give some qualitative idea of the differences between the Ideal MHD model, RCM coupling, and CRCM coupling. In general, the RCM and CRCM coupled models show greater variance in their field-aligned currents and conductances, which is expected as the RCM and CRCM couplings fine tune the magnetospheric variable computations in the Ideal MHD model. All models show the same general trend in FAC and conductivity intensity, that is these values increase dramatically about halfway through the model run. Around 08:45 UT, all the models reach their highest values before beginning to decrease in intensity. The OCB (open-closed field line boundary) stays vaguely circular in shape for the Ideal MHD model, however, with the RCM and CRCM models we see an increase in irregularity of shape. This irregular shape is more on par with the expected behavior of the OCB. Since the OCB tells us the location of the boundary of open magnetic flux forming the polar cap in the Earth's ionosphere, perfect (or near perfect) symmetry rarely occurs.

However, in the CRCM model in particular there often appears to be discontinuity of the OCB which is not necessarily expected and could be an indication of a fault with coupling—most likely related to the mapping between model grids. While this is most prominent in the CRCM model, it also occurs in the RCM model which is why the mapping between grids is suspected as a possible source for the discontinuity (the same mapping is used for both couplings). FAC and electric potential values also appear to share a closer correspondence in the CRCM and RCM models than in the Ideal MHD model as is hoped for since this should be the case.

### 4.2 Lag Time and Interpolated Data

One of the purposes of this study was to describe the relationship between the three couplings and the solar wind conditions and coupling efficiency. SW and IMF conditions are injected at the outer magnetospheric boundary located at 32 $R_E$, however it takes travelling about 20 $R_E$ for the SW conditions to reach the inner boundary where the values in the IM and Ideal MHD models are calculated. Thus, it takes extra time for the solar wind and IMF conditions to propagate and there must be an associated lag time between the solar wind and IMF conditions and the model simulation runs. In order to find the correlation between the solar wind, IMF conditions, and coupling efficiency with the polar cap area and CPCP, it's important to calculate this lag time.

It's expected that a strong correlation will exist between the dayside coupling efficiency and the CPCP and polar cap area values. To find the correlation value, the Ideal MHD model was used as it represents the most basic coupling. In order to find a correlation, however, the data from the injected solar wind and IMF conditions needed to be interpolated to match the values for the couplings. The SW and IMF conditions start ten minutes (at 01:15 UT) later than the actual model run and occur at random intervals separated by a number of seconds. In total, there were 2258 data points for the time interval matching the model runs. The models, however, only occur every five minutes (with 100 data points for the Ideal MHD model) and thus are an entire order of magnitude less in resolution than the SW and IMF values. An interpolation code was created in IDL in order to perform the interpolation between coupling efficiency and the Ideal MHD polar cap areas and CPCPs for both hemispheres.

Once the coupling efficiency data had been interpolated and resolution lowered in order to match the Ideal MHD model data, three different methods were used to find the best lag time. The first method was to find the cross correlation between coupling efficiency and CPCP values for times of 20, 25, 30, 35, and 40 minutes. It's expected that the cross polar cap potential and coupling efficiency will be highly correlated, so the time value with the highest correlation value should correspond to the best lag time value. From this analysis, it was determined that time lag values in the 30-40 minute range gave the best correlations for the Ideal MHD and coupling efficiency in the both the northern and southern hemispheres. Once that had been determined, plots were created to compare the shifted coupling efficiencies with the polar cap area and CPCP graphs in order to do a visual check for correlation and alignment.

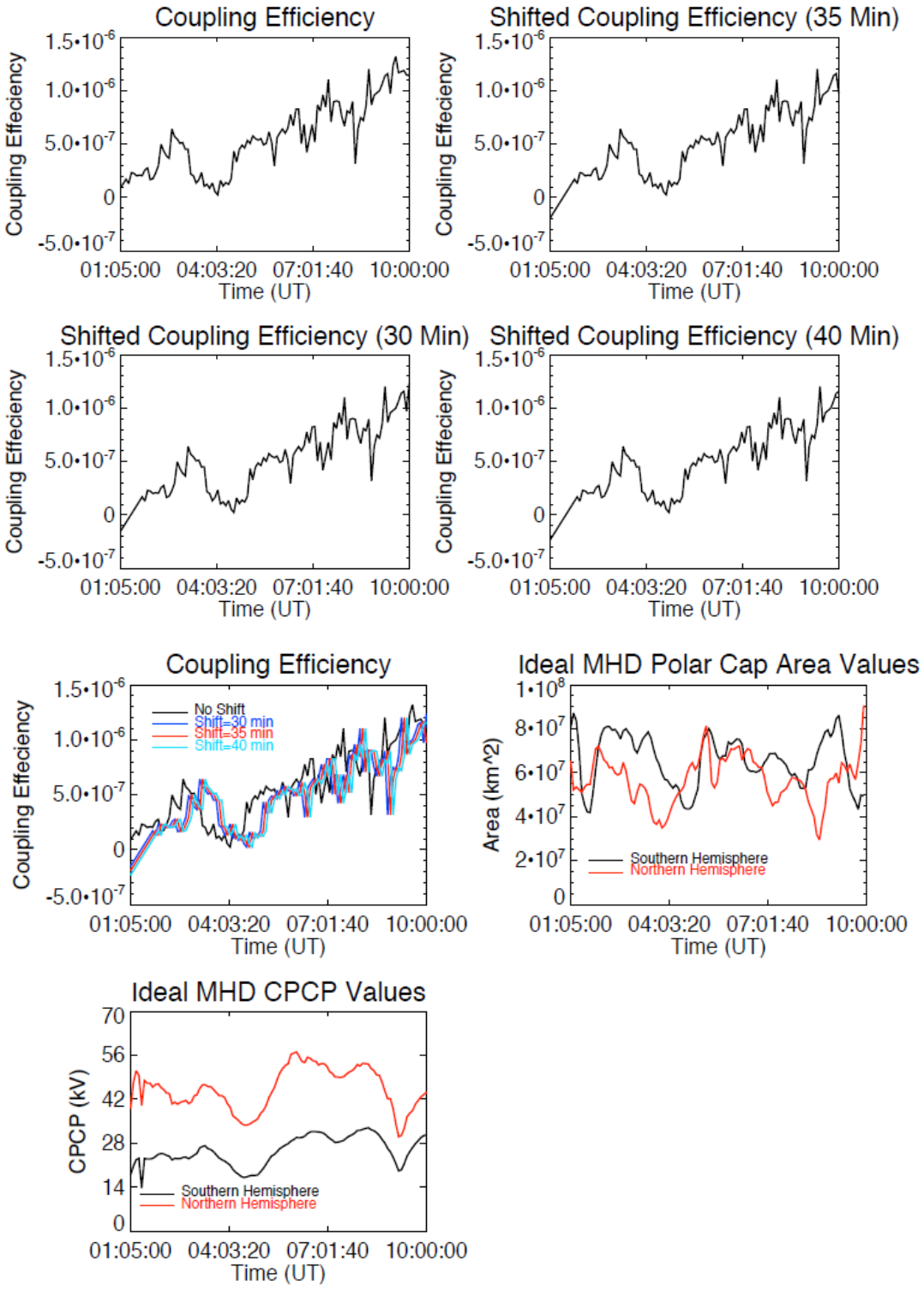


**Figure 24**. Coupling efficiency for lag times of 0, 30, 35, and 40 minutes as well as an over plot of all the lag times.

From the above figures, a visual check seems to indicate that a lag time of 35 or 40 minutes aligns best with the CPCP and polar cap area. In order to find the best lag time, however, a more refined method was necessary. In order to achieve this, cross correlation values were calculated for each model coupling and hemisphere between coupling efficiency and CPCP and polar cap area values. Scatter plots were also generated for each of the runs and will be discussed in the following section 4.5.

| **Northern Hemisphere, CPCP Correlations** | | | |
|---|---|---|---|
| **Lag Times** | **Ideal MHD** | **CRCM Coupling** | **RCM Coupling** |
| **30 Minutes** | p(x,y)=0.2345 | p(x,y)=0.7043 | p(x,y)=0.6143 |
| **35 Minutes** | p(x,y)=0.2497 | p(x,y)=0.7063 | p(x,y)=0.6292 |
| **40 Minutes** | *p(x,y)=0.2638* | *p(x,y)=0.7170* | *p(x,y)=0.6500* |
| **Southern Hemisphere, CPCP Correlations** | | | |
| **Lag Times** | **Ideal MHD** | **CRCM Coupling** | **RCM Coupling** |
| **30 Minutes** | p(x,y)=0.6680 | p(x,y)=0.8250 | p(x,y)=0.7786 |
| **35 Minutes** | p(x,y)=0.6853 | *p(x,y)=0.8231* | *p(x,y)=0.7854* |
| **40 Minutes** | *p(x,y)=0.6940* | p(x,y)=0.8215 | p(x,y)=0.7778 |
| **Northern Hemisphere, Polar Cap Area Correlations** | | | |
| **Lag Times** | **Ideal MHD** | **CRCM Coupling** | **RCM Coupling** |
| **30 Minutes** | *p(x,y)=0.1070* | p(x,y)=0.0477 | p(x,y)=0.1276 |
| **35 Minutes** | p(x,y)=0.0373 | *p(x,y)=0.-0.050* | p(x,y)=0.1340 |
| **40 Minutes** | p(x,y)=0.-0.0048 | *p(x,y)=0.-0.050* | *p(x,y)=0.2020* |
| **Southern Hemisphere, Polar Cap Area Correlations** | | | |
| **Lag Times** | **Ideal MHD** | **CRCM Coupling** | **RCM Coupling** |
| **30 Minutes** | p(x,y)=-0.0346 | *p(x,y)=-0.4460* | *p(x,y)=0.0729* |
| **35 Minutes** | p(x,y)=0.0373 | p(x,y)=-0.4005 | p(x,y)=0.0628 |
| **40 Minutes** | *p(x,y)=-0.0470* | p(x,y)=-0.3732 | p(x,y)=0.0482 |

**Table 1**. Table of correlation coefficients for both hemispheres between dayside coupling efficiency and CPCP and polar cap area values for each of the models. The best correlation in each category is italicized.

Based on the linear Pearson correlation coefficients for each model as well as the previous graphs, the best lag time for the model couplings appears to be forty minutes. However, not all of the correlations are maximized by this lag time. This is due to the assumption made that the lag time for the model runs is constant, however this is not the case. The coupling efficiency is based on the x-direction velocity and y and z components of the magnetic field. As discussed previously, however, these values vary over the time period of the model runs. The x-component velocity varies from a minimum of about -293 to -275 km/s. The y and z component magnetic fields don't have as much variation as the solar wind; the z component does vary from approximately 1.0 to -3.5 nT and the y component varies from around 2.0 to -1.5 nT. Ideally, the time lag would also be varied by sampling the solar wind and IMF conditions at the magnetopause using a simulation instead of the injected values used in this constant lag time analysis. For now, however, the constant lag time of forty minutes was used in the following analyses.

### 4.3 Polar Cap Area

The open-closed field line boundary is the boundary that separates open from closed magnetic field lines. The open magnetospheric field lines are still connected to the solar wind and its associated charged particles, density, temperature, and velocity as it is still entangled with the IMF. Thus, with open field lines the motion of the magnetospheric plasma is affected by the motion of the solar wind. Closed field lines, however, are closed to the IMF and are not affected by SW conditions. The OCB is one of the most important topological features in the magnetosphere and its location is critical to understanding plasma convection processes and it is important that magnetospheric models accurately reflect the boundary location. The polar cap area is defined as the region of the magnetosphere where field lines open to the interplanetary

magnetic field and its boundaries are given by the OCB. Field lines inside these polar caps are the only ones with direct access to the SW and thus the polar cap area directly measures the amount of electric and magnetic flux in the magnetosphere. The OCB was determined in the models by finding the latitude and longitude values when the flux-to-volume ratio $(1/B)$ is zero.

When magnetic reconnection occurs on the dayside of the magnetopause, new fluxes are opened and the polar cap area increases. In contrast, reconnection on the nightside destroys open flux and decreases polar cap area. Thus, it is important to study the rate of change per time of the polar cap area for each of three models as this is a measure of the balance between nightside and dayside magnetospheric processes. When field lines are closed, nightside processes are governed by inner magnetospheric motion and can be altered by pressure, temperature, etc which changes the motion of the plasma. Coupling efficiency is a good quantitative measure of how much the models are controlled by the nightside and dayside processes described above.

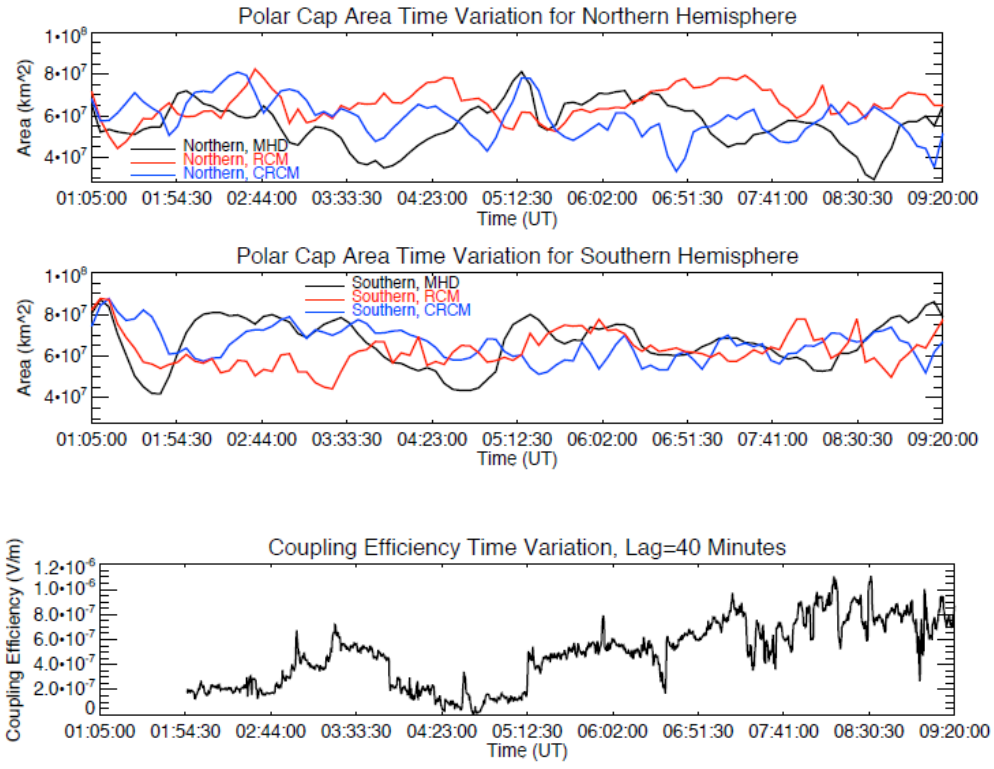


**Figure 25.** Polar cap area over time for each model coupling and hemisphere along with coupling efficiency that has been shifted by 40 minutes to account for lag time

From Figure 25, it's obvious that the polar cap area in the southern and northern hemispheres differ as well as the polar cap areas for each of the three couplings. The southern hemisphere has a greater range in polar cap area values, varying from around $4 \cdot 10^7$ km$^2$ to $8 \cdot 10^7$ km$^2$. Moreover, the southern hemisphere's polar cap areas are, for the most part, larger than the polar cap areas of the corresponding northern hemisphere polar cap areas. The larger variation taking place for the southern polar cap area is suggestive that the southern hemisphere is more susceptible to the affects of the dayside processes--especially in comparison to the northern hemisphere. Since the IMF is oriented southward through most of the model run, increases in the polar cap area are consistent with open flux being created and ongoing low-latitude magnetopause reconnection. The polar cap area can give an indication of how strong the coupling is between the two models. A strong coupling closes open magnetic field lines in the nightside of the magnetosphere and leads to a larger polar cap area. After about 04:30 UT, coupling efficiency steadily increases; however, since the polar cap area in the models does not seem to follow this trend, dayside processes are probably not the most important driving force in the OCB. In order to study this in more detail, scatter plots were created for the polar cap area and interpolated coupling efficiency and correlation coefficients were calculated. Figure 6 on the next page shows the scatter plot and correlation values for each model coupling run.

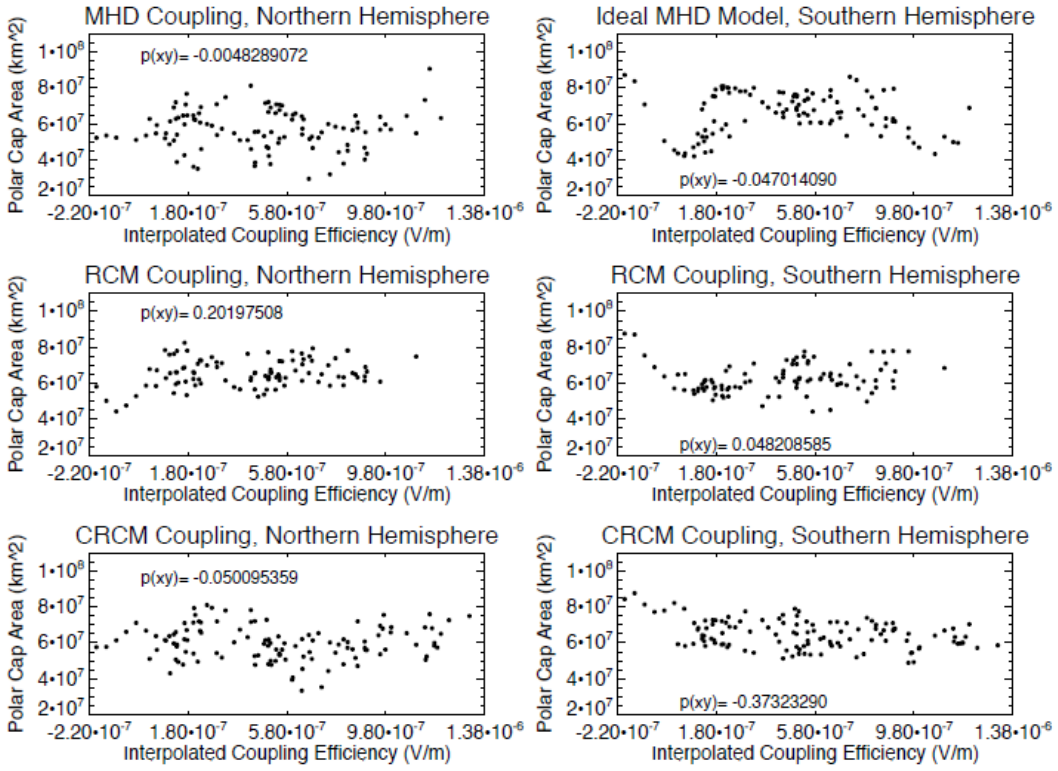


**Figure 26.** Scatter plots of polar cap area and interpolated coupling efficiency.

The above figure shows that there is a weak if not insignificant correlation between all the model couplings' polar cap areas and coupling efficiency. The highest correlations correspond to the RCM coupling in both hemispheres as well as the CRCM coupling in the southern hemisphere. The weak correlation between polar cap area and coupling efficiency in the models suggests that the dayside processes, particularly dayside magnetic reconnection, may not control the magnetospheric models.

It is expected that the CRCM and Ideal MHD models will behave more similarly than the RCM and will follow a similar trend. Looking at the polar cap area plots (Figure 5), however, there are definitely times when the CRCM and Ideal MHD model are at odds. At around 03:30, the polar cap area for the Ideal MHD model in the northern hemisphere is about one order of magnitude less than the CRCM model, while at about 08:45 the opposite can be said. Referring

back to the contour time variation plots in section 5.1, the larger CRCM polar cap areas correspond to times of much larger field-aligned currents, Hall and Pedersen conductivities, and electric potentials. This suggests that the CRCM model could rely more on a least one of these values to drive changes to increase polar cap area along with the dayside opening of fluxes. However, further statistical analysis would be required to make any substantial claims.

### 4.4 Cross Polar Cap Potential (CPCP)

The ionospheric cross polar cap potential (CPCP) is a measure of the change of ionospheric electric potential and measured by $\mathrm{CPCP} = \Delta\Phi = \Phi_{\max} - \Phi_{\min}$ for each time in the model coupling runs. The CPCP is considered to be an instantaneous monitor of the rate at which magnetic flux couples the solar wind to the Earth's magnetosphere-ionosphere system. CPCP should respond linearly to the solar wind's associated electric field and saturate when the IMF's z-component or solar wind becomes very large. The following plots show the solar wind, IMF, and coupling efficiency (shifted by 40 minutes to account for lag time) and the cross polar cap potential for each of the model couplings and hemispheres.

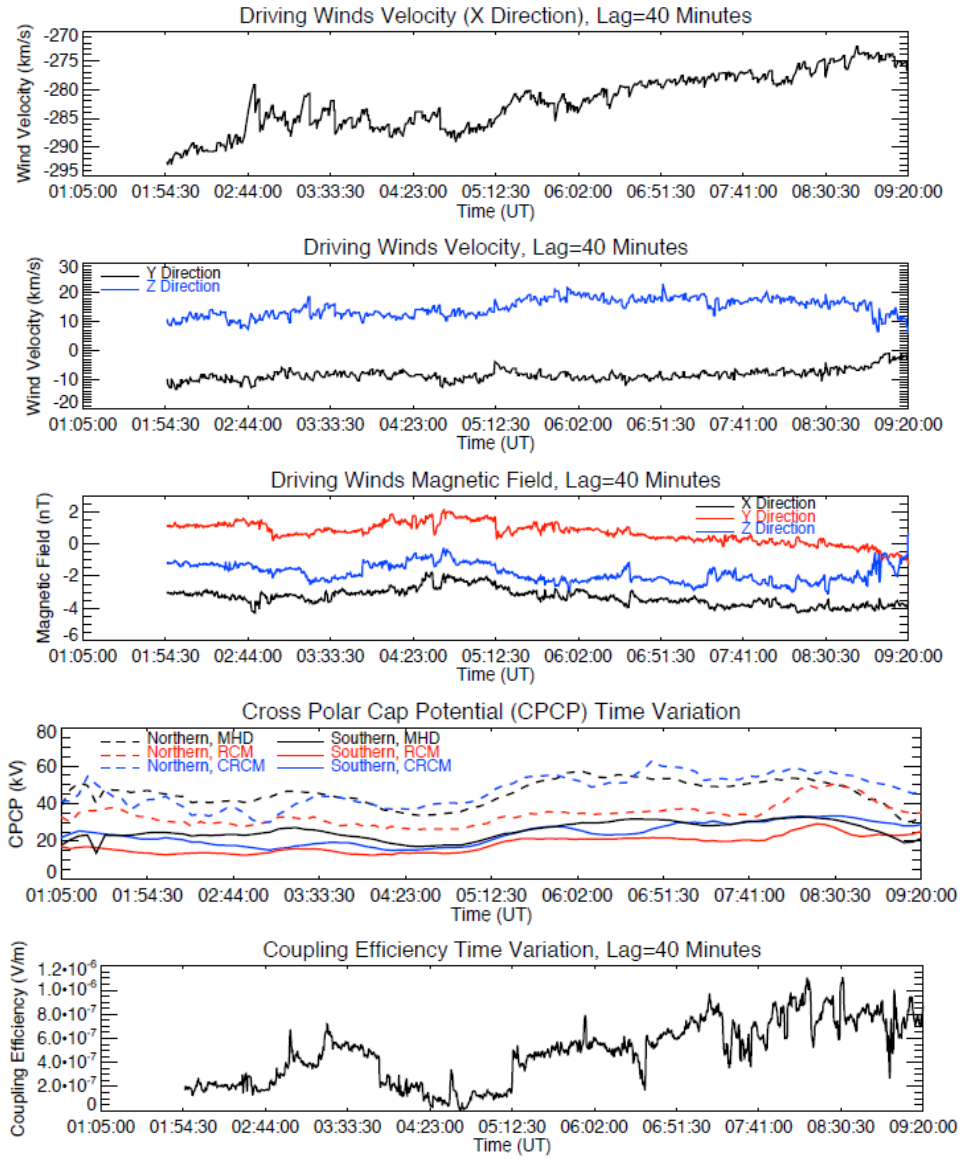


**Figure 27.** Plots of shifted solar wind, IMF, and coupling efficiencies along with the CPCP over the model run times for each model and hemisphere.

If the solar wind is not coupled with the magnetosphere, then the cross polar cap potential will be very low. From the above plots (Figure 7), there are a number of features that stand out. The southern hemisphere CPCP is lower than that of the northern hemisphere due to the season effect--that is since conductance is higher in the southern hemisphere due to the summer season, the associated voltage ($\Delta\Phi$) is lower.

For the CPCP, we see the expected close relationship between the CRCM coupling and Ideal MHD model especially in comparison to the RCM coupling. The RCM coupling is

consistently lower than the CRCM coupling and Ideal MHD model in both hemispheres which suggests that the solar wind is not as well coupled in the RCM model. CPCP increases from about 04:30 to 06:00 UT and decreases from around 08:30 UT until the run is complete. Comparing the representative time plots in section 5.1, shows that the increasing interval corresponds to an increase in FACs and Hall and Pederson conductivities while, conversely, decreasing CPCP corresponds to a decrease in these values. This suggests a proportional relationship between the CPCP and conductance and FACs as expected. Polar cap area can also be compared to the CPCP relationship. From 04:30 to 06:00 UT, when CPCP is increasing in both Ideal MHD and CRCM coupling, the Ideal MHD model decreases then sharply increases while the CRCM decreases steadily. Likewise, for the interval 08:30 to 09:20 UT when CPCP is decreasing, the Ideal MHD model increases sharply and the CRCM model decreases sharply. Based on these qualitative measurements there might be an inverse relationship between the Ideal MHD polar cap area and CPCP values, however it appears that the CRCM coupling's CPCP and polar cap areas are not related. However, quantitative measurements need to be made in order to assess the validity of this claim.

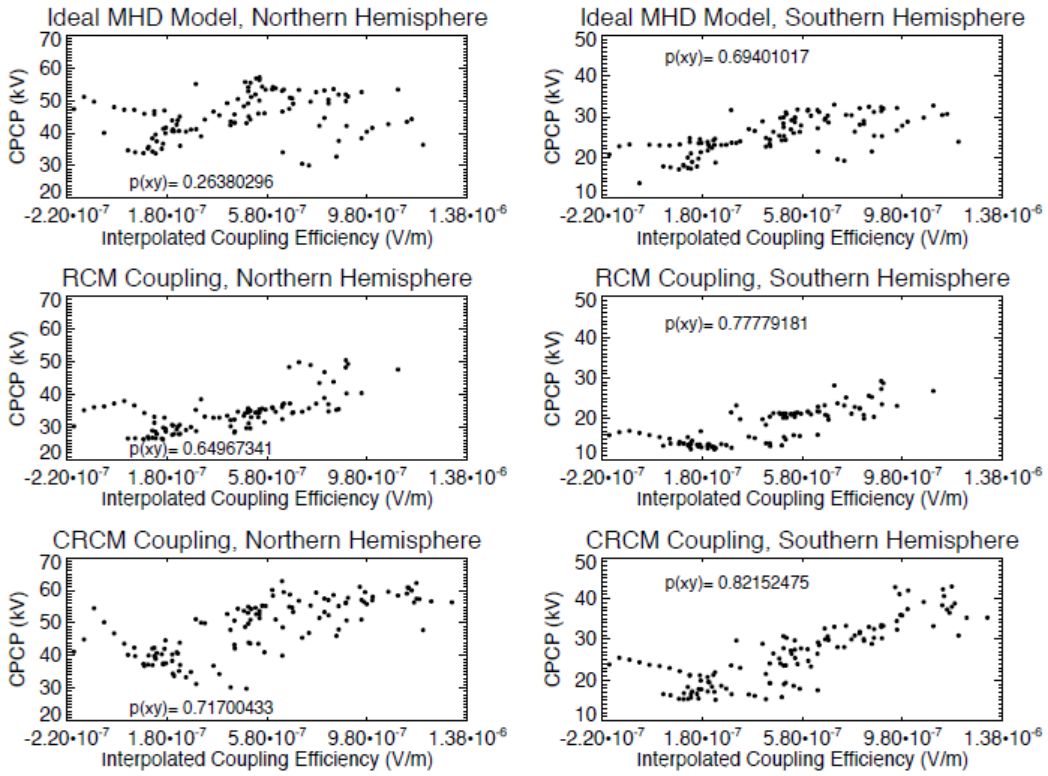


**Figure 28.** Scatter plots of CPCP and interpolated coupling efficiency.

Since the model couplings are run during quiet geomagnetic times, the CPCP should give a good reflection of the coupling efficiency with solar wind. Also, inner magnetospheric processes are not as important during quiet times and thus will not contributes significantly to the model outputs. Figure 8 (above) shows decently strong correlations between coupling efficiency and CPCP values over the model run times with the exception of the Ideal MHD northern hemisphere model. The stronger the coupling efficiency's correlation with CPCP values, the lesser the effect of the inner magnetospheric processes on the model coupling output. In general, the correlations are strongest in the southern hemisphere and in the CRCM. This leads to the conclusion that the inner magnetosphere plays more part in the southern magnetospheric processes. It could also mean that the CRCM is a better indicator of IM values than the RCM model and could make a better IM coupling model.

## 5. Conclusions

There are a number of factors which must be considered before deciding which model performs best during quiet geomagnetic times. It is obvious in any case that the basic model in use—the Ideal MHD—falls short in each of the comparison categories. In the case of the time representative plot, variable values did not have as high a range as for the CRCM and RCM couplings. This is to be expected since the coupling of an IM model necessarily fine-tunes the global model by incorporating ring current and IM convection processes. Through this incorporation, more features are made apparent that are otherwise left out of the basic model. Moreover, the symmetrical nature of the OCB in the Ideal MHD model is a problem. While the OCB may very well have a symmetrical shape, the shape should show more variation with time. In the case of the CRCM and RCM couplings, this occurs showing that the models are responding better to SW and IMF driving conditions. Correlation values between the coupling efficiency and CPCP and polar cap area were also weakest for the ideal MHD model in each hemisphere which is suggestive of a weaker coupling.

While the RCM and CRCM couplings provide a better global model than the Ideal MHD alone, differences between the CRCM and RCM models are also apparent. The time variation plots show some similarities between the two and using them here for a basis of comparison is difficult. One thing that stands out, however, is the discontinuities in the OCB in both the CRCM and RCM. These discontinuities should not occur and it is possible that they are an error from the mapping from the 2D grids used in both the CRCM and RCM models and the 3D BATS-R-US grid. This problem is much more apparent in the CRCM model which could indicate a deeper problem than the one in the RCM. While the RCM shows a stronger correlation between coupling efficiency and polar cap area in the northern hemisphere, the CRCM model shows a

stronger correlation between coupling efficiency and CPCP and polar cap area than the RCM model in all other cases which could indicate that it is the stronger IM model between the two.

## 6. Future Work

Once of the first things to be done in the future is to determine a time lag that varies with the solar wind and IMF conditions to get a better idea of the real correlation between the driving solar wind, IMF, and coupling efficiency with the polar cap area and CPCP values. Further analysis is also needed to understand whether the Hall and Pedersen conductivities, field-aligned currents, or electric potential have a larger effect on the CRCM model than the Ideal MHD model's OCB. Also useful would be to quantify the correlation between these values and all of the model couplings.

This model comparison was done for quiet geomagnetic times to lay a basis for such comparison. However, disturbances can be caused by coronal mass ejections (CMEs) or co-rotating interaction region (CIR) of the SW that can drive geomagnetic storms. When these disturbances occur, the inner magnetospheric processes become more important in the magnetosphere and the IM components will have a greater effect on the overall coupled output. Thus, these times are more interesting and important to the comparison between the three couplings. Future work needs to be completed to repeat the analysis at such times of geomagnetic disturbances. Furthermore, this analysis stressed the ionospheric responses for a global idea of the magnetosphere. More future work could be done to better examine the magnetospheric processes. Studying these would give a better idea of ionosphere-magnetosphere interactions and exchange which would enhance the model comparisons.

## References


Blanc, M., and A. D. Richmond (1980), The ionospheric disturbance dynamo, *J. Geophys. Res., 85*, 1669-1686.

Buzulukova, N., M. -C. Fok, A. Pulkkinen, M. Kuznetsova, T. E. Moore, A. Glocer, P. C. Brandt, G. Tòth, and L. Rastätter, Dynamics of ring current and electric fields in the inner magnetosphere during disturbed periods: CRCM-BATS-R-US coupled model, *J. Geophys. Res., 115,* A05, 210, doi: 10.1029/2009JA014621.

De Zeeuw, D., S. Stanislav, R. Wolf, T. Gombosi, A. Ridley, and G. Tòth (2004), Coupling of a global MHD code and an inner magnetospheric model: Initial results, *J. Geophys. Res, 109,* A12219, doi: 10.1029/2003JA010366.

De Zeeuw, D. L., T. I. Gombosi, C.P. T. Groth, K. G. Powell, and Q. F. Stout (2000), An adaptive MHD method for global space weather simulations, *IEEE Trans. Plasma Sci., 28*, 1956-1965.

Fejer, B. G., R. W. Spiro, R. A. Wolf, and J. C. Foster (1990), Latitudinal variation of perturbation electric fields during magnetically disturbed periods: 1986 SUNDIAL observations and model results, *Ann Geophys., 8*, 441-454.

Folk, M.-C., R. A. Wolf, R. W. Spiro, and T. E. Moore (2001), Comprehensive computational model of Earth's ring current, *J. Geophys. Res., 106*, A5, 8417-8424, doi: 10.1029/2000JA000235.

Forbes, J. M., and M. Harel (1989), Magnetosphere-thermosphere coupling: An experiment in interactive modeling, *J Geophys. Res., 94*, 2631-2644.

Goodman, M. L. (1995), A three-dimensional, iterative, mapping procedure for the implementation of an ionosphere-magnetosphere anisotropic Ohm's law boundary condition in global magnetohydrodynamic simulations, *Ann. Geophys., 13*, 843-853.

Glocer, A., M. Fok, X. Meng, G. Toth, N. Buzulukova, S. Chen, and K. Lin (2013), CRCM+BATS-R-US two way coupling, *J. Geophys. Res.,108*,1635-1650, doi: 10.1002/jgra.50221.

Powell, K.G., P.L. Roe, T.J. Linde, T. I. Gombosi, and D.L. De Zeeuw (1999), A solution-adaptive upwind scheme for ideal magnetohydrodymamics, *J. Comput. Phys.*, 154(2), 284-309.

Rae, I. J., et al. (2010), Comparison of the open-closed separatrix in a global magnetospheric simulation with observations: the role of the ring current, *J. Geophys. Res, 115*, A08216, doi: 10.1029/2009JA015068.

Rae, I. J., K. Kabin, R. Rankin, F. R. Fenrich, W. Liu, J. A. Wanliss, A. J. Ridley, T. I. Gombosi, and D. L. De Zeeuw (2004), Comparison of photometer and global MHD determination of the open-closed field line boundary, *J. Geophys. Res, 109*, A01204, doi: 10.1029/2003JA009968.

Ridley, A. J., T. Gombosi, and D. De Zeeuw (2004), Ionospheric Control of the magnetosphere: conductance, *Ann. Geophys., 22*, 567-584.

Ridley, A.J., D. L. De Zeeuw, T. I. Gombosi, and K. G. Powell (2001), Using steady-state MHD results to predict the global state of the magnetosphere-ionosphere system, *J. Geophys. Res., 106*, 30, 067-30, 076.

Ridley, A.J. T.I. Gombosi, and D. I. De Zeeuw (2004), Ionosphere control of the magnetosphere: Conductance, *Ann. Geophys, 22*, 567-584.

Sazykin, S. Y. (2000), Theoretical studies of penetration of magnetospheric electric fields to the ionosphere, Ph.D. thesis, Utah State University, Logan, Utah.

Stout, Q. F., D. L. De Zeeuw, T. I. Gombosi, C .P. T. Groth, H. G. Marshall, and K. G. Powell (1997), Adaptive blocks: a high-performance data structure, paper presented at Supercomputing 1997 Conference, IEEE Comput. Soc., San Jose, Calif.

Tòth, G., et al. (2005), Space Weather Modeling Framework: A new tool for the space science community, *J. Geophys. Res.,110,* A12226, doi: 10.1029/2005JA011126.

Tòth, G., et al. (2012), Adaptive numerical algorithms in space weather modeling, *J. Comput. Phys., 231,* 807-903, doi:10.1016/j.jcp.2011.02.006.

Vasyliunas, V. M. (1970), Mathematical models of magnetospheric convectionand its coupling to the ionosphere, in *Particles and Fields in theMagnetosphere*, edited by B. M. McCormack, pp. 60 – 71, D. Reidel, Norwell, Mass.

Winglee, R. M. (1994), Non-MHD influences on the magnetospheric current system, *J. Geophys. Res., 99,* 13, 437-454.

Wolf, R. A. (1983), The quasi-static (slow-flow) region of the magnetosphere, in *Solar Terrestrial Physics*, edited by R. L. Carovillano and J. M. Forbes, pp. 303– 368, D. Reidel, Norwell, Mass.